Scilight

Highlights in High-Energy Physics
https://www.sciltp.com/journals/hihep

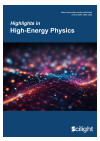

Review

Probing Beyond the Standard Model with Gravitational Waves from Phase Transitions

Chiara Caprini [1,2]

[1] Theoretical Physics Department, CERN, 1211 Geneva, Switzerland; chiara.caprini@cern.ch
[2] Département de Physique Théorique, Université de Genève, 1211 Genève, Switzerland

How To Cite: Caprini, C. Probing Beyond the Standard Model with Gravitational Waves from Phase Transitions. *Highlights in High-Energy Physics* **2025**, *1*(3), 22. https://doi.org/10.53941/hihep.2025.100022

Received: 11 November 2025
Revised: 25 December 2025
Accepted: 30 December 2025
Published: 31 December 2025

Abstract: This review article is based on a seminar presented at the Higgs pairs workshop 2025. Stochastic gravitational wave backgrounds can serve as probe of the diverse phenomenology encountered in beyond-Standard-Model scenarios featuring phase transitions in the early Universe. Focussing on gravitational wave production from first-order phase transitions, we present the main results of a recent analysis by the LISA Cosmology Working Group concerning the detectability of such signals with LISA. Strong degeneracies, both among the parameters controlling the phase transition and between these and the parameters of the beyond-Standard-Model scenario underlying the phase transition, complicate the reconstruction of the model from a potential signal. Nonetheless, once a specific scenario is assumed, LISA observations can supply constraints possibly complementary to those obtainable from present and future particle colliders.

Keywords: early universe; gravitational waves; phase transitions

1. Introduction

Because of the weakness of the gravitational interaction, the Universe is "transparent" to gravitational waves (GWs) throughout its evolution. Indeed, particles with weaker interactions decouple from thermal equilibrium at correspondingly higher energy scales: supposing a weak interaction cross section for gravitons of the type $\sigma \sim G^2T^2$ where G is the Newton constant, providing an interaction rate $\Gamma(T) = \sigma\, n\, v \sim G^2T^5$ where n is the particle's number density at thermal equilibrium $n \sim T^3$, and $v = 1$ (we work with units $\hbar = c = k_B = 1$), the condition for thermal equilibrium in the early Universe reads $\Gamma(T)/H(T) \sim G^2T^5/(T^2/M_{\rm Pl}) \sim (T/M_{\rm Pl})^3$, where $H(T)$ is the Hubble factor and $M_{\rm Pl}$ the reduced Plank mass [1]. This shows that gravitons are decoupled at temperatures smaller than the Planck scale. Therefore, GW emission processes in the early Universe form a fossil radiation, similarly to the Cosmic Microwave Background (CMB), but whose detection has the potential to bring direct information from stages of the Universe's evolution to which we have no access through electromagnetic radiation, photons getting out of thermal equilibrium at the much lower temperature $T_{\rm dec} \simeq 0.26$ eV [2]. For example, such a fossil GW radiation could be generated in the phase of thermal evolution of the Universe comprised between the end of Inflation and Big Bang Nucleosynthesis (BBN). The detection of such a signal might constitute a direct observational probe of processes like reheating after Inflation, spontaneous symmetry breakings, baryogenesis, the production of dark matter.

GW signals from the early Universe have therefore an amazing discovery potential in cosmology, comparable to the one of the CMB sixty years ago, but linked to higher energies. This naturally raises the question of whether they can be used as a new probe of high energy physics, complementary to particle colliders. The answer depends both on the capabilities of the available GW observatories, and on the characteristics of the potential GW sources. As we will show, current GW observatories are serendipitously well suited to probe most interesting energy scales in the early Universe, provided that appropriate sources exist with the right features (see e.g. [3–5]), and that the challenges related to the detection of the signal can be properly addressed (see e.g. [6–13]).

This review article is based on a seminar given at the Higgs pairs workshop 2025, and focusses on the generation

of GWs from first-order phase transitions (PTs), possibly occurring in the early Universe. PTs are a compelling GW source, with diverse consequences and relevant connections with high energy physics. After a description of the general properties of the GW signal in Section 2, mainly based on [3], in Section 3 we briefly overview possible GW sources linked to PTs, as well as some of the proposed beyond-Standard-Model (BSM) scenarios realising them. In Section 4 we focus on first-order PTs. In Section 4.1 we briefly review some of the main GW generation processes operating at first-order PTs, as well as the features of the GW signal: this section is based on [14]. In Section 4.2 we discuss in particular the case of the Electroweak (EW) symmetry breaking, testable by LISA, and review the results on the detectability of this signal obtained in the last work of the LISA Cosmology Working Group on this topic, Ref. [15]. This work also assessed the capabilities of LISA to constrain two particular scenarios of first-order PTs that are particulary compelling: we review these results in Section 4.3. We conclude in Section 5. The background metric of the Universe is the Friedmann Lemaître Robertson Walker (FLRW) metric $ds^2 = -dt^2 + a^2(t)dx_i dx^i$ and GWs are inserted at first-order in cosmological perturbation theory.

2. Motivation: Characterisation and Detection of Stochastic GW Backgrounds

Let us consider a GW generating process operating during the radiation dominated, thermal equilibrium phase in the early Universe, at a temperature T_* and over a short time interval, typically less than one Hubble time $H(T_*)^{-1}$. It is natural to assume that this process has a characteristic length scale that is bounded, by causality, by the Hubble length: $\ell_* \leq H(T_*)^{-1}$. This length scale corresponds to an angular size on the sky today $\Theta_* = \ell_*/d_{A,*} \leq H(T_*)^{-1}/d_{A,*}$, where $d_{A,*}$ is the angular diameter distance [2]. For example, the angular scale corresponding to the Hubble scale at the epoch of photon decoupling $T_{\rm dec} \simeq 0.26\,{\rm eV}$ is $\Theta_{\rm dec} = H(T_{\rm dec})^{-1}/d_{A,{\rm dec}} \simeq 0.9$ deg, as measured by the first peak of the CMB angular power spectrum [2]. As motivated in the introduction, interesting GW generation processes typically operate at higher energy scales, i.e. earlier times, than photon decoupling: therefore, the angular scales corresponding to their correlation scales are typically much smaller. For example, a GW signal produced by a process operating at the EW energy scale would be correlated on the sky today on an angular scale $\Theta_*(T_* \simeq 100\,{\rm GeV}) \simeq 10^{-12}$ deg; if produced at the QCD energy scale, it would be correlated on $\Theta_*(T_* \simeq 100\,{\rm MeV}) \simeq 10^{-9}$ deg [3]. These angular scales are way smaller than the typical angular resolution of GW detectors on the sky, which is $\Delta\Theta \sim (fL)^{-1}$ with f the sensitivity frequency and L the detector baseline: for example, for LISA it is about 10 deg (see e.g. [16]). Consequently, GW detectors measure the GW signal from the superposition of many uncorrelated regions on the sky, and thereby can only access its statistical properties. Therefore, from the point of view of GW detectors, the signal coming from sources operating in the early Universe takes the form of a stochastic GW background (SGWB), and the tensor metric perturbation $h_{ij}(\mathbf{x}, t)$ must be treated as a random variable.

The latter is in general assumed to be statistically homogeneous and isotropic (because of the symmetries of the FLRW Universe), unpolarised (if the generation process does not violate parity) and Gaussian (because of the central limit theorem). The most immediate way to characterise the present-day signal is therefore through its power spectral density $S_h(f)$,

$$\langle h_r(f, \hat{\mathbf{k}}) h_p^*(g, \hat{\mathbf{q}}) \rangle = \frac{1}{8\pi}\, \delta(f-g)\, \delta^{(2)}(\hat{\mathbf{k}} - \hat{\mathbf{q}})\, \delta_{rp}\, S_h(f) \tag{1}$$

where $h_r(f, \hat{\mathbf{k}})$ are the coefficients in the plane wave expansion $h_{ij}(\mathbf{x}, t) = \int_{-\infty}^{+\infty} df \int d\hat{\mathbf{k}}\, h_r(f, \hat{\mathbf{k}}) e^r_{ij}(\hat{\mathbf{k}})\, e^{2\pi i f(t - \hat{\mathbf{k}}\cdot\mathbf{x})}$, and we sum over the polarisations $r = +, \times$. The bracket $\langle ... \rangle$ in Equation (1) denotes the ensemble average over the random variable, which can be substituted with volume (or time, from the point of view of the detector) average under the ergodic hypothesis, as customary in cosmology. We consider the present-day signal as a superposition of plane waves, since the source active in the early Universe has long ceased. In the cosmological context, rather than $S_h(f)$, one often uses $\Omega_{\rm GW}(f)$, the power spectrum of the GW energy density per logarithmic frequency interval, normalised by the critical energy density of the Universe today ρ_c:

$$\frac{\rho_{\rm GW}}{\rho_{\rm c}} = \frac{\langle \dot{h}_{ij}(\mathbf{x}, t) \dot{h}^{ij}(\mathbf{x}, t) \rangle}{32\pi G\, \rho_c} = \int_0^{+\infty} \frac{df}{f}\, \Omega_{\rm GW}(f)\,, \quad \text{with } \Omega_{\rm GW}(f) = \frac{\pi}{2} \frac{f^3 S_h(f)}{G\, \rho_c} \tag{2}$$

The spectral shape of $\Omega_{\rm GW}(f)$ depends on the properties of the GW source. In the case under analysis of a GW source operating over a short time interval during the radiation dominated era and characterised by the length scale ℓ_*, the GW signal has a characteristic frequency $f_* \sim 1/\ell_*$. The fractional GW energy density power spectrum $\Omega_{\rm GW}(f)$ typically peaks at this frequency, redshifted to today:

$$f_0 = f_* \frac{a(T_*)}{a(T_0)} = \frac{1.65 \times 10^{-5}}{\ell_* H_*} \left(\frac{g(T_*)}{100}\right)^{\frac{1}{6}} \frac{T_*}{100\,\mathrm{GeV}}\,\mathrm{Hz} \tag{3}$$

where we have expressed f_0 in terms of the dimensionless ratio $\ell_* H_* \leq 1$, $a(T)$ is the scale factor and $T_0 \simeq 2.7$ K is the temperature of the Universe today, and $g(T_*)$ denotes the number of relativistic degrees of freedom at temperature T_*. Equation (3) connects the present-day characteristic frequency of a GW signal f_0, with the epoch in the early Universe during which the sourcing process was active, parametrized by T_*. It thus also provides a way to associate each GW observatory - defined by its operational frequency range - with the minimal energy scale in the early Universe to which it is sensitive.

Let us first consider the currently operating network of Earth-based interferometers LIGO, Virgo and KAGRA (LVK) [17–19]. Their frequency range of detection spans $1\,\mathrm{Hz} \lesssim f \lesssim 1000\,\mathrm{Hz}$. Setting $\ell_* H_* = \mathcal{O}(1)$, Equation (3) therefore selects the temperature range $10^6\,\mathrm{GeV} \lesssim T_* \lesssim 10^{10}\,\mathrm{GeV}$. Interestingly, this range corresponds to the energy scale of the Peccei-Quinn PT [20–25] in "post-inflationary" models, within which, the axion decay constant F_a is bounded by $10^{7-8}\,\mathrm{GeV} \lesssim F_a \lesssim 10^{10-11}\,\mathrm{GeV}$ [26–37]. While the detection of a SGWB of cosmological origin by the LVK networks is unlikely, as it will most probably be masked by the astrophysical foreground from stellar mass black hole binaries [38,39], the situation might be entirely different for the planned 3rd generation of Earth-based GW detectors, Einstein Telescope (ET) [40] and the Cosmic Explorer (CE) [41]. These should be operative around the middle of the 2030s, with an expected factor of 20 improvement in sensitivity [42], and the level of foreground from astrophysical sources is expected to be much smaller [43–47]. This opens up the exciting possibility of probing the cosmological $U(1)_{\mathrm{PQ}}$ PT, and thereby exploring a possible solution of the CP problem, with GW detectors [14,48,49].

Moving to lower frequencies, the GW detector that is expected to be first operative is the space-based interferometer LISA, planned for launch around 2035 [50]. LISA will be composed of a triangular configuration of three spacecraft on an heliocentric orbit with 2.5 million km arms, and will be sensitive to the lower frequency range $10^{-5}\,\mathrm{Hz} \lesssim f \lesssim 0.1\,\mathrm{Hz}$ [7]. Again setting $\ell_* H_* = \mathcal{O}(1)$, Equation (3) selects for LISA the temperature range $10\,\mathrm{GeV} \lesssim T_* \lesssim 10^5\,\mathrm{GeV}$. Therefore, LISA offers the possibility to probe the EW energy scale and beyond [51–53]: in particular, as we will show, LISA could probe BSM scenarios in which the EWPT becomes of first-order, possibly in a complementary way to particle colliders [15]. That is, if the SGWB from the early Universe is higher than the numerous foregrounds of astrophysical origin that are expected in the LISA band, both of galactic and extra-galactic nature [54–61].

In the range of yet lower frequencies $10^{-9}\,\mathrm{Hz} \lesssim f \lesssim 10^{-7}\,\mathrm{Hz}$ lies the first observational evidence so far of the existence of a SGWB permeating the Universe. Indeed, in 2024, Pulsar Timing Arrays (PTAs) have announced the presence in their datasets of a common red noise that follows the expected response of pulsars to GWs, the Hellings-Downs correlation [62–65]. This correlation allows to ascribe, with confidence ranging from about 3σ to about 4.5σ depending on the PTA collaboration, the observed red noise to a proper GW signal. The current data will be combined within the International PTAs, and this analysis is expected to turn the evidence into a discovery [66]. An extremely precise characterisation of the SGWB is then expected with the advent of the Square Kilometer Array Observatory [67,68]. The most immediate explanation for this signal consists in the superposition of the GW emission from a population of inspiralling supermassive black hole binaries [69,70]. However, cosmological sources operating in the early Universe are for the moment not excluded: rather, some of them could explain the detection equally well, if not better [69,71–73]. Within this scenario, applying again Equation (3) with $\ell_* H_* = \mathcal{O}(1)$, the selected energy scale for PTAs would correspond to $10\,\mathrm{MeV} \lesssim T_* \lesssim 1\,\mathrm{GeV}$: therefore, PTAs are ideally suited to probe the QCD energy scale. The PTA signal could then be due to GW sources operating in connection with the QCD PT, offering the possibility to probe the conditions under which it actually took place in the early Universe [74–78].

The aforementioned GWs observatories happen to be ideally suited to probe key energy scales in the early Universe. It is imperative to exploit this serendipitous coincidence, given its transformative scientific potential. Moreover, the outlook is particularly promising, as the observational landscape is expected to expand significantly. Additional frequency bands are likely to be explored in the future as new detector concepts mature. For instance, the deci-Hz window could become accessible within the next few decades through proposals based on both laser [79,80] and atom interferometry [81–85], or by measuring Moon's vibrations [86,87]. Lower frequencies than PTAs may also be probed via extremely precise astrometric measurements [88–94]. Most intriguing from the perspective of high-energy physics, however, are detector concepts operating in the MHz-GHz range, which would enable exploration of even more extreme energy scales, potentially reaching those associated with Grand Unification and with reheating after Inflation [95–99].

However, being in the right frequency range alone does not guarantee detection: signals must also lie sufficiently above the observatories' sensitivity limit. This means, that the GW source operating in the early Universe must be sufficiently 'strong'. A rough estimate of the scaling of the SGWB signal amplitude with the characteristics of the source can be obtained from the following simple argument [3]. As before, we assume that the source is operating over a short time interval, and denote its characteristic size ℓ_*. GW are sourced by tensor anisotropic stresses Π_{ij}, that is, the transverse traceless component of the energy momentum tensor of the source. The GW wave equation reads $\ddot{h}_r + 3\,H\,\dot{h}_r + k^2 h_r = 16\pi G\,\Pi_r$, from which one can estimate the GW amplitude scaling as $h \sim 16\pi G\,\Pi\,\ell_*^2$. For this order of magnitude estimate we neglect indices and identify the time evolution of the source with is characteristic length-scale ℓ_*, i.e. we assume a relativistic source. This is indeed a good assumption, as we will see later on. The GW energy density therefore becomes (see the first equality in Equation (2)) $\rho^*_{\rm GW} \sim \dot{h}^2/(32\pi G) \sim 8\pi G\,\Pi^2\,\ell_*^2$. Normalising to the total energy density in the Universe at the time of GW production $\rho^*_{\rm tot} = 3H_*^2/(8\pi G)$, one has $\rho^*_{\rm GW}/\rho^*_{\rm tot} \sim (H_*\ell_*)^2\,(\Pi/\rho^*_{\rm tot})^2$, leading to the GW parameter today (c.f. Equation (2))

$$\Omega_{\rm GW} \sim \Omega_{\rm rad}\,(H_*\ell_*)^2\left(\frac{\Pi}{\rho^*_{\rm tot}}\right)^2 \tag{4}$$

where $\Omega_{\rm rad} = \rho^0_{\rm rad}/\rho_c \simeq 2.47\cdot 10^{-5}$ is the radiation energy density parameter today [100], and we have used the fact that GWs scale as radiation with the evolution of the Universe. The amplitude of the GW signal scales like the square of the source characteristic size normalised by the Hubble scale, and with the square of the amount of anisotropic stresses available to source the GWs, normalised to the energy density in the Universe at the source time. It is important to stress that Equation (4) was obtained under highly simplified assumptions and is not intended to represent the full SGWB signal. Most notably, it does not contain the frequency dependence of the spectrum. Nevertheless, it provides a useful proxy for general considerations. Comparing for example with the sensitivity of LISA $\Omega_{\rm GW} \sim 10^{-11}$ [7], we see that only sources which involve a sizeable fraction of the total energy density in the Universe, and have sizes comparable to the Hubble scale, are strong enough to produce detectable signals: $(H_*\ell_*)(\Pi/\rho_{\rm tot})_* \gtrsim 10^{-3}$. In the next section we describe a class of sources for which these conditions can be met.

3. Gravitational Waves from Phase Transitions in the Early Universe

PTs are one of the phenomena occurring in the early Universe with the richest phenomenology in terms of GW production. Many processes connected to PTs naturally lead to tensor anisotropic stresses and thereby to GWs. We can distinguish two broad classes of GW sources: first-order PTs (for reviews, see e.g. [5, 14, 101, 102]) and PT producing topological defects (for reviews, see e.g. [14, 103–105]).

- **First-order PTs:** in this case, the anisotropic stresses arise from the out of equilibrium processes linked to the first-order PT. In particular, the PT proceeds through the nucleation of bubbles where the field undergoing the PT, typically a scalar field (e.g. the Higgs field), has settled to the true vacuum. Towards the end of the PT, bubbles collide in order to convert the entire Universe to the broken phase. The collisions of the broken phase bubbles breaks the spherical symmetry of the scalar field spatial gradients, and can produce anisotropic stress of the form $\Pi_{ij} \sim [\partial_i\phi\partial_j\phi]^{TT}$, where TT stands for the transverse and traceless projection [106–112]. Since the scalar field is in general coupled to the particles of the surrounding early Universe plasma, the latter is set into motion by the bubble expansion [113–117]. Bulk fluid motion develops in the form of sound waves [118–122] or kinetic turbulence [123–131], leading to anisotropic stresses in the form $\Pi_{ij} \sim [\gamma^2(\rho+p)v_iv_j]^{TT}$, where ρ and p are the energy density and pressure of the fluid, and γ the Lorentz factor (relativistic motion is typically favourable to large GW production). Finally, large-scale electromagnetic fields can be induced along with the bubble dynamics and/or the bulk fluid motion, that naturally possess anisotropic stress: $\Pi_{ij} \sim [-E_iE_j - B_iB_j]^{TT}$ [132–136]. These can be due, for example, to electromagnetic currents generated by particle separation at the bubble walls [137–139], and can get then amplified up to equipartition with the kinetic turbulence energy. Another important source of GWs in first-order PTs can arise if the vacuum energy gets released into particle production rather than bubble walls dynamics [140, 141]. The anisotropic stresses sourcing GWs are then those associated to the out of equilibrium particle distribution function [142, 143].
- **Topological defects:** in this case, the topological defects are directly the cause of the tensor anisotropic stresses sourcing the GWs [144–147]. Topological defects may form when a symmetry is spontaneously broken, and their nature depends on the topology of the vacuum submanifold [103–105, 148]: for example, if it is disconnected, domain walls may form, or if it contains loops which cannot be shrunk to a point, cosmic strings may form. These are the two cases most studied in the literature. The properties of the defects are determined by the action of the theory: of particular importance are for example their stability, the energy per unit length/surface, their interactions. Both cosmic strings and domain walls form a network in the

Universe that produces all types of metric perturbations [144,149], among which also tensor perturbations, i.e. GWs [150]. In the case of local strings-arising e.g. from the spontaneous breaking of a local $U(1)$ symmetry [103, 104], the closed loops are the strongest source of GWs, as opposed to the infinitely long strings extending outside the Hubble scale [151–153]. Global strings, on the other hand, mainly decay via particle production [154–163]. Both cosmic strings and domain walls networks evolve reaching a scaling regime. However, while the energy density in the cosmic strings network always remains a constant fraction of the Universe energy density, the decay of domain walls is instead very slow [103,164]. One must therefore introduce an annihilation mechanism in the domain walls model, acting before the domain walls network comes to dominate the Universe expansion: for example, a small explicit breaking of the discrete symmetry inherent to the domain walls [165,166]. This means that domain walls are in general a short-lived source, and their GW signal follows the prescription of Equation (4); while cosmic strings source GW throughout the Universe evolution, and therefore their GW signal does not satisfy the scaling of Equation (4).

A general condition that must always be satisfied, both in the case of GW production by first-order PTs and by topological defects, is that the homogeneity and isotropy of the Universe observed at large scale by the CMB must be maintained. In the first case, the anisotropic stresses can reach an important fraction of the Universe energy density, but in general this occurs at small scales, and over a short amount of time, with respect to the Hubble length/time. CMB limits are then safe. In the second case, the metric perturbations induced at large scales by the string or domain wall network must satisfy CMB constraints [167,168]. Given the weakness of the gravitational interaction, the sourced SGWB is always far below the upper bounds on the radiation energy density derived by the CMB or BBN [3].

The PTs known in the context of the Standard Model (SM) do not lead to any appreciable GW production. Both the EWPT and the QCD PT are predicted to be cross-overs [169–175], and no other PT leading to topological defects is expected within the SM. GWs are indeed produced by the SM plasma in thermal equilibrium [176], but their amplitude is too small to be of observational relevance, given the capabilities of proposed GW detectors so far [96]. Consequently, observational evidence of the presence of first-order PTs and/or topological defects in the early Universe constitutes a significant test of new physics. Several scenarios have been explored, that could provide this observational evidence in the form of GWs, sometimes even with other, very relevant, associated signatures, such as the presence of dark matter candidates, baryogenesis, and solutions to the hierarchy problem:

- **EW sector extensions:** one of the most notable example of such scenarios are BSM extension of the EW sector. Despite the absence of observational indication of new physics near the EW energy scale, many scenarios leading to a first-order EWPT remain viable. They mainly rely on extending the SM with light scalars, that can alter the Higgs potential producing a barrier either at tree level or perturbatively. One can for example directly add a gauge singlet scalar field coupling at tree level to the SM Higgs field, possibly endowed with a $\mathbb{Z}_2$ symmetry that could make it stable and thereby contribute a Dark matter candidate [177–197]. In the latter case, the PT can proceed in two steps [180,181]. Another scenario leading to a first-order EWPT proposes to extend the SM Higgs sector with scalar EW multiplets, as for example in the model featuring two Higgs doublets [198–210], or with a triplet [211–215]. Going beyond minimal extensions, albeit constrained, SUSY models provide a UV-complete theory that predicts new light particles which effect could be to change the order of the EWPT, such as for example in singlet/multiplet extensions of the MSSM [216–221].
- **Effective approach:** a different approach, adapted to the case in which the new physics influencing the EWPT is at higher energy than the EW scale, is to represent the heavy new physics by effective higher dimensional operators [222–226]. This allows to study the impact of heavy BSM extensions without worrying about a specific theory. The Higgs potential is modified by adding new terms of higher power of the Higgs field, suppressed by the scale of the new physics. Whether this approach can correctly capture the EWPT features in complete theories depends on the model, however, it is clear that by adding those operators the EWPT can become strongly first-order [227–231].
- **New symmetries:** moving away from the EW symmetry breaking, a minimal extension of the SM via a local $U(1)_{B-L}$ symmetry is also very interesting, since it can possibly explain the neutrino masses, provide dark matter candidates in the form of right-handed neutrinos, explain the baryon asymmetry of the Universe via leptogenesis and lead to detectable GWs since the PT of the $U(1)_{B-L}$ symmetry breaking in the early Universe tends to be strongly first-order due to the classical conformal invariance [232–238].
- **Conformal models:** going beyond the scenarios of weakly coupled theories with polynomial potentials, there are models featuring strong dynamics such as warped extra-dimensions [239–249] and composite Higgs models [223,224,250–253]. In both cases, the confinement PT associated with the spontaneous breaking of the conformal invariance is strongly first-order, and in composite Higgs scenario it can be naturally linked to the EW one.

- **Dark sectors:** strong first-order PTs can arise in the context of dark sectors, which motivate the existence of dark matter (eluding any observation other than based on its gravitational interaction) within a more complete theory. Dark sectors only interact with the SM through a portal, and feature all possible kinds of new interactions and symmetries: they can therefore very naturally host strong first-order PTs [254–267]. Particularly interesting are models in which the first-order PT is required for other phenomenological reasons, such as producing the baryon asymmetry, stabilising the dark matter candidate or providing the right relic abundance [258,264,265,268–270].
- **QCD and heavy axions:** proposed long ago to solve the strong CP problem, the Peccei Quinn model is a well motivated BSM model with concrete applications [20–25]. The axion, arising as a pseudo-Nambu-Goldstone boson from the breaking of the $U(1)_{PQ}$ symmetry, can be a stable dark matter candidate; furthermore, this model can lead to a variety of GW sources. Indeed, the spontaneous breaking of the $U(1)_{PQ}$ symmetry can be realised via a strong first-order PT, directly sourcing GWs [14,24,25,35,48,271,272]. Furthermore, this model also features the formation of topological defects, including global cosmic strings from the $U(1)_{PQ}$ symmetry breaking (which mostly decay via emission of axions) but also of domain walls, produced when the $U(1)_{PQ}$ is broken to a discrete symmetry [49,273], which are particularly interesting for GW production in the context of heavy axion models [274–288]. To avoid domain wall domination, an explicit breaking of the discrete symmetry is needed, introducing a vacuum non-degeneracy that makes the domain wall annihilate [273,289]. This is one of the few models in which topological defects can lead to a detectable GW signal other than those in which the defects are generated by the spontaneous breaking of higher symmetry patterns connected to Grand Unified Theories.
- **QCD PT:** it is also important to mention that, although the QCDPT is also predicted to be a cross-over, this result has been obtained from lattice simulations run at zero baryon and charge chemical potentials, as appropriate within the SM. However, the actual conditions in which the PT took place in the early Universe might be different, for example the lepton asymmetry in the Universe is much less constrained than the baryon one, and could be large, which might lead to a change in the order of the QCDPT [290–293].

A still open question, subject of interesting ongoing research, is to which level perturbative treatments of the finite temperature potential in first-order PTs can be considered accurate, given that in many scenarios the barrier is not present at tree level, but induced by radiative and/or finite-temperature corrections. A promising direction is to implement dimensional reduction, a resummation technique based on matching to a three-dimensional effective field theory, allowing non-perturbative treatments of the PT in the associated four-dimensional theory and thereby improved precision of the finite temperature dynamics [5,189,294–304].

The brief and necessarily incomplete overview of GW-producing scenarios given above already illustrates their remarkable diversity. It is important to emphasise, however, that in many cases the resulting GW signal, despite arising from highly non-trivial processes, exhibits too few distinctive features to unambiguously discriminate between the different underlying scenarios. This is because the signal typically depends only on the gross properties of the tensor anisotropic stresses that source it, such as their typical time and length scales, rather than on the details of the high-energy physics scenarios producing them. In the following, we aim at illustrating this point with a concrete example, focusing in particular on GWs generated during first-order PTs.

4. Focus on First-Order Phase Transitions

In the previous section, we have provided a very concise summary of some of the best motivated BSM scenarios that can lead to sizeable GW signals, because they involve first-order PTs and/or the formation of topological defects. Given the variety of models, the question naturally arises whether it is possible to distinguish, from the detection of the GW signal, one scenario from the other. In the following we present the results of [15], in which an attempt is made to answer this question specifically for the case of a first-order PT occurring at the EW energy scale, considering its observability by the LISA interferometer.

4.1. Gravitational Wave Sources Operating at a First-Order Phase Transition

A first-order PT, in particular if related to the EW symmetry breaking, must complete within one Hubble time, so that the entire Universe settles in the new vacuum of the theory. Furthermore, as explained in Section 3, the anisotropic stresses are connected to the collision of bubbles: the GW source therefore has a well defined associated length scale, the size of the bubbles at collision, which is smaller than the Hubble scale at the PT time H_*^{-1}. Therefore it seems plausible that a first-order PT, as a GW source, fulfils the criteria of applicability of Equation (4). Let us start working from this hypothesis.

The characteristic size of the GW source in this case is given by $\ell_* \sim v_w/\beta$, where v_w denotes the bubble

wall velocity, and β is the transition rate parameter, which can be evaluated directly from the action $S(t)$ [305–308]. Within the assumption of exponential nucleation, the probability of tunnelling per unit volume and time can be written as $\Gamma(t) = \Gamma(t_*)\exp[(\beta(t-t_*)]$, with $\beta = \frac{d}{dt}S(t)\big|_{t_*}$, where t_* denotes a reference time, which in this case should be chosen around the time of bubble percolation (for more detail, see the discussion on T_* later in this section) [309–311]. The inverse timescale β can be used as a proxy for the inverse duration of the PT (for more detail, see e.g. [14]).

The bubble wall velocity, also entering in $\ell_* \sim v_w/\beta$, is notoriously difficult to estimate. This quantity links the microscopic scales of the problem - it depends on the effective potential, i.e. the pressure difference in the two phases, and on the interaction of the particles with the bubble wall, i.e. with the field undergoing the PT - to the macroscopic scales of the problem, i.e. the bubble size, and the collective plasma dynamics at this size. Indeed, the fluid profile around the wall depends on the bubble wall velocity. In the case of thermal PTs, it is often assumed that the bubble quickly reaches a steady state, characterised by a constant wall velocity given by the balance between the driving force (the pressure difference in the two phases) and the friction force (due to the interaction of the wall with the particles in the surrounding plasma) [114,122,312–315]. One then solves the fluid equations of motion imposing conservation of energy and momentum across the bubble discontinuity, and finds the fluid velocity and enthalpy profiles surrounding the bubble [114] (implemented e.g. in the tool `CosmoGW` [316], see also [317]). It is possible to adopt a phenomenological description introducing a macroscopic friction parameter, in principle covering several particle theory models. However, it is very challenging to properly model the bubble wall velocity given the variety of possible BSM scenarios and its high model dependence [117,190,318–331]. Therefore, v_w is mostly assumed as an input in studies of the GW signal, despite the fact that the signal does depend quite strongly on its actual value.

As presented in Section 2, the characteristic size of the GW source ℓ_* determines the characteristic frequency of the SGWB f_*, which in turns connects to the frequency of the signal today f_0 through the temperature T_*, representing the epoch in the early Universe during which the GW source was active, see Equation (3). Note that Equation (3) assumes that the Universe was in thermal equilibrium and in the radiation dominated phase. This means, that the PT must already have completed, or be about to complete, at T_*. Since the GW sourcing is due to the collision of the bubbles, and therefore takes place towards the end of the phase transition (in the case bulk fluid motion, even after the PT completion, as we will see), this assumption is reasonable. One option is then to associate to T_* the percolation temperature, i.e. the ambient temperature when a connected group of bubbles spans the entire universe [5,332]. Another option, particularly adapted to the case of exponential nucleation, is to associate T_* to the time t_* at which the fractional volume in the metastable phase has reached $P(t_*) = 1/e$, so that roughly 63% of the Universe is converted to the broken phase [311]. The two times are close, since $P(t_{\rm perc}) = 0.71$ [5,332]. In the absence of substantial supercooling, the radiation component dominates the Universe's evolution throughout the PT, which, furthermore, must occur within one Hubble time: the percolation temperature is then close to both the critical and the nucleation temperatures, and the conversion between time and temperature can be performed using Friedmann's equation for a radiation dominated Universe. Conversely, in the case of substantial supercooling, the Universe is dominated by the vacuum energy for a short period of time: the critical, nucleation and percolation temperatures may substantially differ, and it is therefore important to distinguish them and to identify T_* as close to the latter. Since, during the short inflationary phase, the volume is rapidly expanding, one further needs to ensure that the fractional volume which is still in the false vacuum is decreasing at percolation time, so that the PT can complete [309,332]. Moreover, thermal equilibrium must be re-established via a reheating process: the easiest option is then to postulate that the latter is instantaneous, such that the Hubble rate during the vacuum dominated phase (and in particular at percolation) is the same as the Hubble rate in the thermal phase following the PT, H_* [14,116,331,333]. Within this setting, T_* can be unambiguously identified.

The other important term in Equation (4) is the anisotropic stress energy fraction $\Pi/\rho^*_{\rm tot}$. One usually defines the GW source energy fraction $K = \rho_s/\rho^*_{\rm tot}$, where ρ_s denotes the energy density of the GW sourcing process, and $\rho^*_{\rm tot}$ denotes the total energy density in the Universe at the PT time, assumed to be radiation to derive Equation (4). When the anisotropic stresses are due to the colliding bubble walls, ρ_s is the gradient energy in the scalar field, which we denote ρ_φ. When the anisotropic stresses are due to the bulk fluid motion caused by the coupling between the bubble wall and the surrounding plasma, ρ_s is the kinetic energy of the bulk fluid motion, which we denote ρ_v. The PT is a dynamical process in which the free energy of the system, given by the effective potential at finite temperature, is transformed mainly into thermal energy (with no associated anisotropic stress), and in small part into gradient energy of the bubble walls and kinetic energy of the fluid. In the following, we always make the assumption that the equation of state of the system can be described by the the bag equation of state, and that the sound speed of the fluid is constant and fixed to $1/\sqrt{3}$. Then, the relative importance of the potential to the thermal energy is

given by the parameter $\alpha = \Delta V_0/[\pi^2 g(T_*)T_*^4/30]$, where ΔV_0 denotes the potential difference at zero temperature between the symmetric and broken phases. α is interpreted as a measure of the PT strength. The efficiency with which the potential energy is transformed into gradient energy of the bubble walls or kinetic energy of the fluid is given by the efficiency parameters $\kappa_{\varphi,v} = \rho_{\varphi,v}/\Delta V_0$, so that the GW source energy fraction can be written as $K = (\kappa_\varphi + \kappa_v)\alpha/(1+\alpha)$. The efficiency parameters are in general calculated using for $\rho_{\varphi,v}$ the gradient/kinetic energy density of a single bubble [114].

The parameter α governs which process, among the scalar field gradients or the bulk fluid motion, dominates the GW production:

- If the PT is strong, $\alpha \gtrsim \mathcal{O}(1)$ and the vacuum energy is equal or larger than the relativistic fluid energy: the PT entails some amount of supercooling, possibly a short inflationary phase. Bubbles are assumed to accelerate until the speed of light, and the dominant GW source is bubble collisions. The anisotropic stresses in the scalar field energy momentum tensor are due to the breaking of the spherical symmetry connected to the bubble collisions [106–112,115–117].
- If the PT is weak, $\alpha \lesssim \mathcal{O}(10^{-2})$ the potential energy is subdominant, and the GW production is dominated by the fluid motion. Since the PT is weak, so are the velocity/enthalpy perturbations in the fluid generated by the expanding bubble walls: the system is characterised by the development of sound waves, which surround the bubbles [118–122]. The superposition of sound waves following bubble collision leads to the breaking of the spherical symmetry and the presence of anisotropic stresses in the fluid energy momentum tensor. Remarkably, sound waves remain in the fluid for long after the bubble walls are collided. They therefore continue sourcing GWs for many Hubble times, an important qualitative difference with respect to bubble collision.
- If the phase transition is of moderate strength, $\alpha \sim \mathcal{O}(0.1) - \mathcal{O}(1)$, the GW production is still dominated by fluid motion, however, the velocity/enthalpy perturbations in the fluid can be high, leading to non-linear compressional and vortical turbulence, possibly of the magnetohydrodynamic (MHD) type, i.e. accompanied by magnetic fields. The chaotic superposition of fluid velocity typical of turbulence then leads to non-zero anisotropic stresses in the fluid energy momentum tensor [76,123–131]. As well as sound waves, turbulence also continues to source GWs for many Hubble times, after the bubbles are gone.

Note that the GW source energy fraction K as defined in the literature and above, differs from the anisotropic stress energy fraction $\Pi/\rho_{\rm tot}^*$. It is indeed very difficult to estimate what fraction of the gradient energy in the scalar field, or of the bulk kinetic energy, is in the form of anisotropic stresses, efficient in sourcing GWs. The reasons are multiple. For example, in the case of anisotropic stresses from bubble collisions, they depend on the particular realisation of the collision process. Although analytical estimates exists [111,112,330], the best way to tackle this is through numerical simulations of the bubble nucleation process, possibly capturing also the microscopic scale corresponding to the bubble wall, in order to study the scalar field dynamics at and after bubble collisions [108–110,115,117,334,335]. If the anisotropic stresses are sourced by bulk fluid motion, the latter sources GW for long after the bubbles have collided, so the memory of the actual collision realisation is erased. However, the difficulty still stands in the fact that the bulk fluid motion can become highly non linear, especially in the case of moderately strong PTs. Again, analytical estimates exists [76,122–125,127,129,131,336–340], but it is imperative to validate them with numerical simulations of the fluid dynamics [119–121,128,130,341–350].

Therefore, in general, numerical simulations are necessary to properly model the GW signal, because of the intrinsic randomness of the process, of the complicated fluid shells profiles surrounding the bubbles, of the non-linear fluid dynamics. At this stage, we can rewrite Equation (4) in a more realistic way:

$$\Omega_{\rm GW}(f) \sim \Omega_{\rm rad}\,\tilde{\Omega}_{\rm GW}\,K^2\,\mathcal{F}(H_*\ell_*)\,S(f) \tag{5}$$

The above equation still does not capture all the complexity of the SGWB signal, but conveys some more information than Equation (4). First of all, to follow conventions, we have rewritten $\Pi/\rho_{\rm tot}^* = \tilde{\Omega}_{\rm GW}\,K^2$, where $\tilde{\Omega}_{\rm GW}$ parametrises the efficiency with which the energy fraction K is converted into anisotropic stresses actually sourcing the GWs. This parameter must in general be determined via numerical simulations (for more detail, see e.g. [344] and references therein). Second, we have inserted the generic function $\mathcal{F}(H_*\ell_*)$ to express the fact that the scaling as $(H_*\ell_*)^2$ can be modified in the case of bulk fluid motion, since this kind of process, contrary to bubble collisions, can source GWs for a time longer than a Hubble time, deviating from the conditions under which Equation (4) was derived. At last, we have reinserted the frequency dependence in $\Omega_{\rm GW}(f)$ (c.f. Equation (1)), the normalised SGWB power spectrum $S(f)$. For more detail on the scaling and properties of the SGWB signal, see e.g. [14].

Numerical simulations allow to predict the SGWB from the different sources operating during a first-order PT in detail. In particular, they allow to link the PT strength to the actual energy available in the GW source,

that is to provide estimates of the efficiency parameters $\kappa_{\varphi,v}$, and in turns of K. As previously mentioned, the efficiency parameters are in general evaluated from the single bubble solution: numerical simulations allow to check whether this is a good assumption. This is still very much work in progress, but discrepancies with the analytical single-bubble solution are often found [120, 342–344]. Furthermore, numerical simulations provide insight on which sources, among bubble collision, sound waves and turbulence, dominate the GW production, and how they are connected among each other. They also predict the signal amplitude and its spectral shape $S(f)$. Each source produces power spectra with different features, such as different peaks and slopes, and it is necessary to be able to link these features to the actual GW source and to the PT parameters, for a correct interpretation of the signal. In this respect, complementing numerical results with analytical understanding is of great help. Detailed predictions of the SGWB signals are still much work in progress. Several numerical codes exist that tackle the problem with different approaches: for example, numerical simulations performed with the SCOTTS code [119–121, 131, 341] include the scalar field dynamics and the relativistic fluid motion, but not the expansion of the Universe neither the magnetic field; numerical simulations performed with the Pencil code [128, 130, 345–347, 351] include the expansion of the Universe and the magnetic field, but no scalar field; Higgsless simulations [342–344] are the least computationally expensive, but rely on steady state solutions for the bubble expansion. Constant progress is being made by the community in refining SGWB predictions, in particular in the most relevant case of strong first-order PTs.

In the following, we do not discuss the detailed form of the SGWB spectral shape $S(f)$. The precise determination of $S(f)$ depends on the specific GW sourcing mechanism: bubble collision, sound waves, (MHD) turbulence. Much like the scaling of the signal with the PT parameters, this remains an active area of research, combining input from analytical approaches and numerical simulations. Reviews of this topic have been attempted, for example, in the analyses of the LISA Cosmology Working Group [15, 52, 53], where expressions for $S(f)$ are proposed that capture the main qualitative features of the frequency dependence for the various GW sources. However, providing an unified description that encompasses all possible dependencies and variations of $S(f)$ across different sourcing scenarios remains extremely challenging [14]. This review is based on the results of Ref. [15], which are obtained adopting state-of-the-art proposals for the signal spectral shape.

4.2. Detecting Signals from a First-Order EWPT at LISA

The GW signal is determined by the dynamics of the PT and of the surrounding plasma, and can in principle be computed in the context of specific PT models. In practice, however, this evaluation involves many complex steps, and it is subject to significant uncertainties. Nevertheless, it is still worthwhile to investigate the question of signal detectability using the information currently available, acknowledging that the resulting predictions inevitably carry intrinsic uncertainties.

Within state of the art SGWB signal modelling, the following parameters enter in the GW signal (a table summarising the key parameters can be found in Appendix A):

- T_*, the energy scale of the PT (to be identified with the temperature around percolation, see discussion in Section 4); α the PT strength; β/H_* the inverse PT duration, normalised to the Hubble rate at the PT time. These parameters can be determined directly by the effective potential, and can be subject to large uncertainty when related to a specific model, e.g. due to the accuracy of perturbative treatments, or in the case of important supercooling.
- v_w, the bubble wall velocity. This parameter depends on the finite-temperature effective potential and the interaction of the scalar field with the particles in the theory, and determines the fluid profile around the wall. Is has been calculated only in some specific models, and is in general fixed to a constant value, often arbitrary, possibly introducing inaccuracy in the GW signal prediction.
- K, the GW source energy fraction. This parameter is determined by the bubble expansion dynamics and the bubble interaction with the surrounding fluid. In most cases, it is evaluated from the efficiency factors $\kappa_{\varphi,v}$ and α, under the assumption that the bubble wall settles to a steady state and adopting the fits of Ref. [114]. This introduces some inaccuracy in estimating the GW signal, because the effect of collisions and possibly non-linearities developing in the fluid dynamics can significantly alter K with respect to the single bubble solution.
- ϵ, the fraction of kinetic energy in bulk motion that is converted to MHD turbulence. This parameter is inserted to represent the fact that, if the PT is strong, non-linearities in the bulk fluid develop, likely leading to the onset of turbulence and possibly to the amplification of magnetic fields. Accurately simulating PTs of adequate strength to follow the formation and evolution of (MHD) turbulence, and thus to reliably predict the resulting GW signal, remains extremely challenging. Although rapid progress is being made in the development of numerical codes (see the simulations performed in [121] and in particular the approach developed in [343, 344]), current simulations are still unable to robustly determine the fraction of energy transferred into (MHD) turbulence as a

function of the PT properties, such as its strength. Consequently, the actual value of ϵ and its dependence on the other PT parameters are not yet known, and ϵ must be treated as a free parameter.

Figure 1, taken from [14], shows the reach of several GW observatories in the two-dimensional parameter space T_* and β/H_*, considering the SGWB generated by a strong first-order PT with $\alpha \gg 1$. In this simple case, the dominant GW source is bubble collisions, so that $\kappa_\varphi \simeq 1$, and therefore $K = \kappa_\varphi \, \alpha/(1+\alpha) \simeq 1$. Furthermore, the bubbles expansion can accelerate to the speed of light $v_w \simeq 1$, and there is no bulk motion, neither in the form of sound waves nor turbulence, therefore $\epsilon = 0$. In [14], detectability is assessed in terms of the signal-to-noise ratio (SNR), the colour shading in Figure 1. Two SNR contours are shown for each GW observatory: the dashed one has been produced accounting only for the instrumental noise, while the dotted one takes into account also the extra noise due to astrophysical foregrounds. Specifically, for the future Earth-based interferometers Einstein Telescope and Cosmic Explorer, the foregrounds are due to the mergers of compact binaries, mainly stellar mass black holes and neutron stars (note that the currently operating interferometers LIGO, Virgo, KAGRA are not yet sensitive enough to detect any astrophysical foreground). For LISA, the main foregrounds are due to the in-spiral of compact binaries (stellar mass black holes, neutron stars and white dwarfs) both within the Milky Way and extra-galactic. In particular, the galactic foreground dominates the LISA noise curve in the frequency range nearby the mHz. For PTAs, accounting for the capability of the future radio telescope Square Kilometre Array Observatory, the foreground, from the point of view of cosmological signal detection, is given by the in-spiral of super-massive black hole binaries. A detailed description of the foregrounds and references can be found in [14]. From Figure 1 it is clear that the presence of foregrounds can significantly affect the sensitivity of GW observatories to a possible cosmological signal. Nevertheless, presently operating devices have already started delving into the parameter space: the gray regions show both the exclusion region from the non-observation of the SGWB from a strong first-order PT by the LVK network [352], and the parameters space region that could account for the NANOGrav 15-years data, if the SGWB is interpreted as arising from a first-order PT [73]. Incidentally, the temperature ranges inferred, for each GW observatory, from the intersections of the SNR curves with the $\beta/H_* = 1$ axis, reflect the energy scales at which each detector can probe GW sources, as discussed in Section 2.

From Figure 1, one sees that at least part of the strong first-order PT parameter space lies within the reach of current and future GW observatories. However, detectability of the signal does not by itself guarantee that the underlying parameters can be reconstructed from the measurement. Within the caveats and uncertainties discussed above, most of the parameters entering the SGWB signal are known, once a PT model is specified and complemented by numerical simulations of the plasma dynamics. Therefore, extracting these parameters from an observation would be extremely valuable, as it would enable to identify the physical origin of the GW signal from its detection.

Ref. [15] investigated the parameter-reconstruction capabilities of LISA and found that, for sufficiently strong signals, the underlying parameters can in principle be inferred. However, the resulting uncertainties are often large, owing to the strong degeneracies in the way these parameters affect the SGWB. These degeneracies can be appreciated in the example provided in Figure 2, where the dependence of the SGWB from sound waves and MHD turbulence on the parameters listed above is shown. For example, K enters in the SGWB amplitude; however, $(H_*\ell_*)$ also strongly affects the amplitude, making it difficult to disentangle the effect of the two parameters (note that, in Figures 2 and 4, the parameter ℓ_* is denoted R_*, since these figures are taken from Ref. [15] and therefore follow the notation convention used in that analysis). Furthermore, $(H_*\ell_*)$ determines the SGWB peak frequency; however, T_* does as well, introducing another source of degeneracy.

To partially alleviate these degeneracies, Ref. [15] proposes an alternative parametrisation of the SGWB signal in terms of features of its spectral shape, rather than in terms of the thermodynamic PT parameters discussed above. In this approach, the SGWB from bubble collisions, which has the form of a broken power law, is characterised by the frequency of its spectral peak, f_b and by the value of the SGWB amplitude at the peak, Ω_b. The SGWBs from sound waves and MHD turbulence, which instead follow double broken power laws, are parametrised by the two break frequencies (f_1, f_2) (with one corresponding to the spectral maximum) and by the amplitude at the second break, Ω_2. These quantities are referred to as "geometric parameters", in contrast to the thermodynamic parameters of the PT described above. Reconstruction in terms of geometric parameters is significantly more tractable, and the degeneracies can be largely removed when the signal is sufficiently strong. Ref. [15] forecasts the regions of geometric parameter space that LISA will be able to measure with better than 10% precision. While the geometric parameters do not directly encode the physical properties of the PT, they are extremely useful for reconstructing the SGWB from LISA data; once measured, they can subsequently be translated back into constraints on the thermodynamic PT parameters, as shown in Figures 3 and 4. Unfortunately, the translation to the thermodynamic parameters brings back the degeneracies.

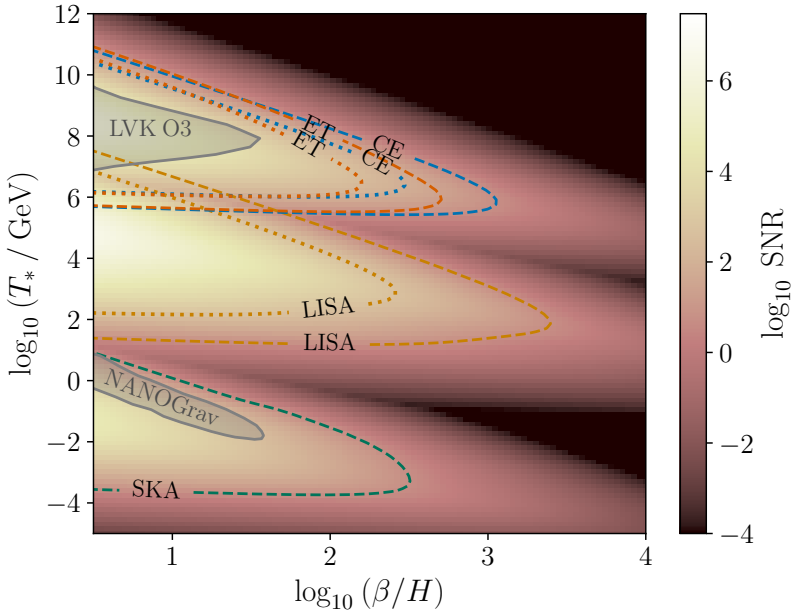

Figure 1. Taken from [14]. This figure shows the maximum signal to noise ratio (colour shading) among four GW observatories (PTAs with the SKA, LISA, Einstein Telescope and Cosmic Explorer) of the SGWB generated by a strong first-order PT in the parameter space given by the PT temperature T_* and the inverse PT duration, β/H_*. The dashed lines show the SNR=5 curves for each detector, evaluated based on the detector noise only, without accounting for the presence of astrophysical foregrounds. The dotted lines show instead the SNR contours of the astrophysical foregrounds relevant in each detector's frequency range. More detail on the population of astrophysical sources taken into account for each detector is given in the main text. Within the region delineated by the dotted contours, the SNR of the cosmological signal exceeds the one of the foregrounds, and the former should therefore be readily detectable. Within the region bounded by the dashed contours, detection may still be achievable, depending on the detailed spectral shape of the cosmological signal. In the case of Einstein Telescope and Cosmic Explorer, the foregrounds lie below the detectors' noise, while for LISA the Galactic foreground component is higher than the detector noise, hence the reduction in accessible parameter space due to the foreground is larger (c.f. [14] for more detail). For PTA, there is no dotted curve as the foreground corresponds to the SGWB that has been detected, and one should refer to the gray contour instead. Indeed, the gray contours denote the 95% confidence exclusion region from LVK non-detection of a SGWB [352], and the 95% confidence region if the PTA NANOGrav signal is interpreted as originating from a strong first-order PT [73]. The temperature intervals inferred from the intersection of the SNR curves of the different observatories with the $\beta/H_* = 1$ axis correspond to those discussed in Section 2, representing the energy scales in the early Universe at which each observatory can probe GW sources.

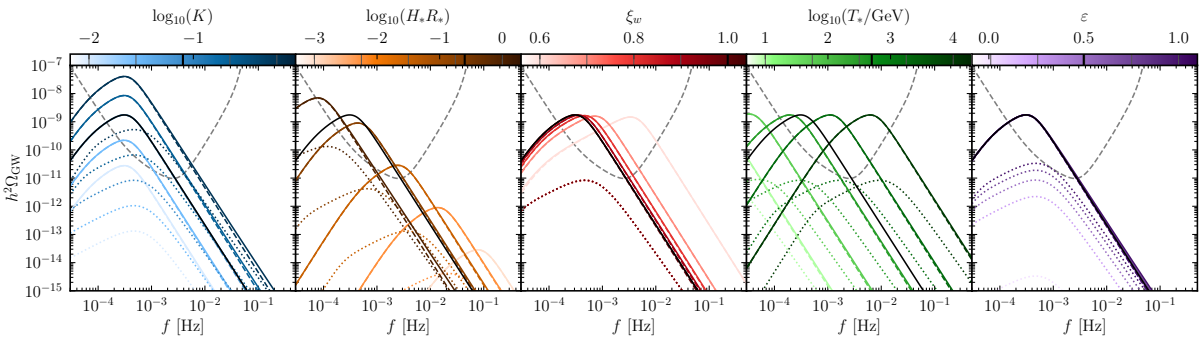

Figure 2. Taken from [15]: SGWB power spectra from sound waves (dashed, coloured lines), MHD turbulence (dotted, coloured lines), and total, given by the sum of the two (solid, coloured lines), as a function of frequency. The black line in each panel shows the SGWB for the benchmark values of the parameters $K = 0.08$, $H_*\ell_* = 0.25$ (the notation of [15] is such that $R_* = \ell_*$), $v_w = 1$ (the notation is such that $\xi_w = v_w$), $T_* = 500$ GeV, $\epsilon = 0.5$. In each panel one parameter is varied around the benchmark value, while the others are kept fixed. The value of the varying parameter can be inferred from the colour shading of the horizontal bar. The gray dashed line appearing in each panel shows the forecasted noise curve of the LISA instrument.

The parameter reconstruction analysis of Ref. [15] is performed on simulated data produced by the `SGWBinner` code [353,354], in the three orthogonal Time Delay Interferometry channels (A,E,T), assuming stationarity and Gaussianity for all data components, which include: (i) the noise of the LISA instrument, simulated starting from a noise model with two free parameters (A, P) where A represents the test mass acceleration noise and P represents the optical metrology noise (the instrument noise at fiducial values for (A, P) is shown by the gray dashed line in Figure 2); (ii) two astrophysical foregrounds, the one from in-spiralling binaries in the Milky Way (mainly white dwarf binaries), and the one from extra-galactic, in-spiralling stellar mass black hole binaries: both are simulated starting from simple template-based predictions; (iii) finally, the SGWB signal, simulated starting from three benchmark spectral shapes describing the signal due to, respectively, bubble collision, sound waves and MHD turbulence, and depending on the above listed thermodynamic parameters. The reconstruction is performed using Markov Chain Monte Carlo sampling of the likelihood by the SGWBinner code, using Cobaya [355], which implements the nested sampler Polychord [356,357] and analyses the samples with GetDist [358]. The sampled parameters are the noise parameters (A, P), with fiducial values $A = 3, P = 15$; the amplitudes of the galactic and extra-galactic foregrounds $(\Omega_{\rm Gal}, \Omega_{\rm Ext})$, with fiducial values $\log_{10}(h^2\Omega_{\rm Gal}) = -7.84$ and $\log_{10}(h^2\Omega_{\rm Ext}) = -12.38$; and the SGWB parameters that vary depending on the case at hand. Information on the priors can be found in [15].

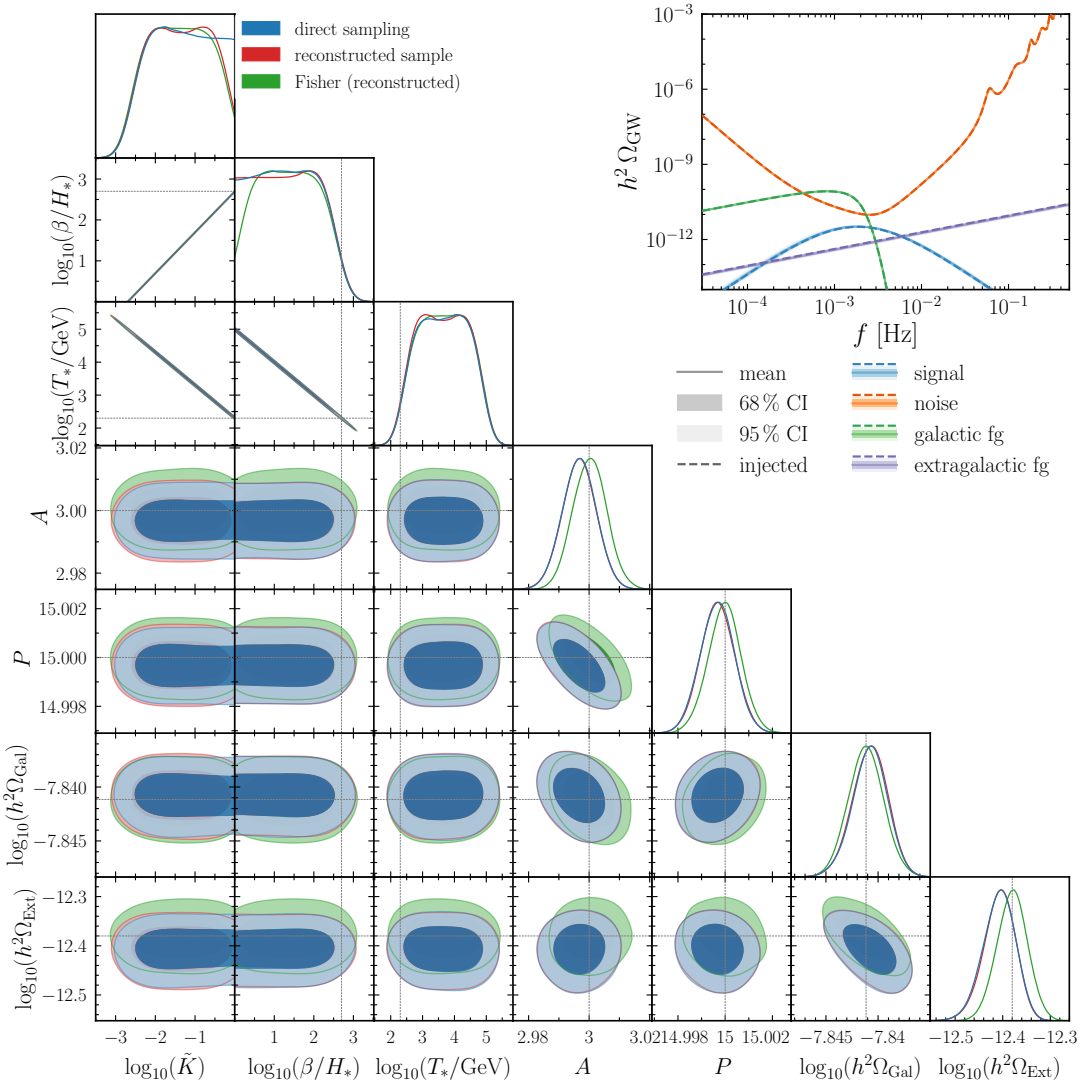

Figure 3. Taken from [15]: Template-based reconstruction of the thermodynamic parameters of a SGWB from bubble collisions at a strong first-order PT, together with the noise and foregrounds parameters. The posteriors of the direct sampling in terms of the thermodynamic parameters are shown in blue. The background red contours are reconstructed from a sample in terms of the geometric parameters of the broken power law, translated to thermodynamic parameters. The green contours are obtained from a Fisher analysis in terms of the geometric parameters, also translated to the thermodynamic parameters. The inset shows the injected noise, foregrounds and signal (dashed lines according to the legend), and their the reconstruction (shaded areas around the dashed lines).

In Figures 3 and 4 we show two examples of reconstruction of the thermodynamic parameters taken from [15]. Figure 3 shows the case of a strong first-order PT, for which the thermodynamic parameters are $(K, T_*, \beta/H_*)$. The input values for the latter have been fixed to $K = 1$, $T_* = 200$ GeV and $\beta/H_* = 500$. While the parameters of the instrument noise and the foreground amplitudes are reconstructed relatively well, strong degeneracies appear in the signal parameters. Nevertheless, a detection is made, in the sense that $K = 0$ is not compatible at more than 95%. Figure 4 shows the case of a SGWB due to both sound waves and MHD turbulence, for which the two parameters v_w and ϵ add to those of the previous case. The input values are $\log_{10} K = -1.1$, $\log_{10}(\ell_* H_*) = -0.6$, $\log_{10}(T_*/\mathrm{GeV}) = 2.7$, $v_w = 1$, $\epsilon = 1$. Large parameter degeneracies are still present, but the reconstruction performs better than in the bubbles collision case. This is because the SGWB spectrum is richer in features such as spectral breaks and different slopes (cf. Figure 2), which help to break some of the degeneracy. Naturally, this improvement make sense within the idealized, template-based framework of Ref. [15]; in a more realistic data-analysis setting, reconstructing a more complex spectral shape is generally more challenging.

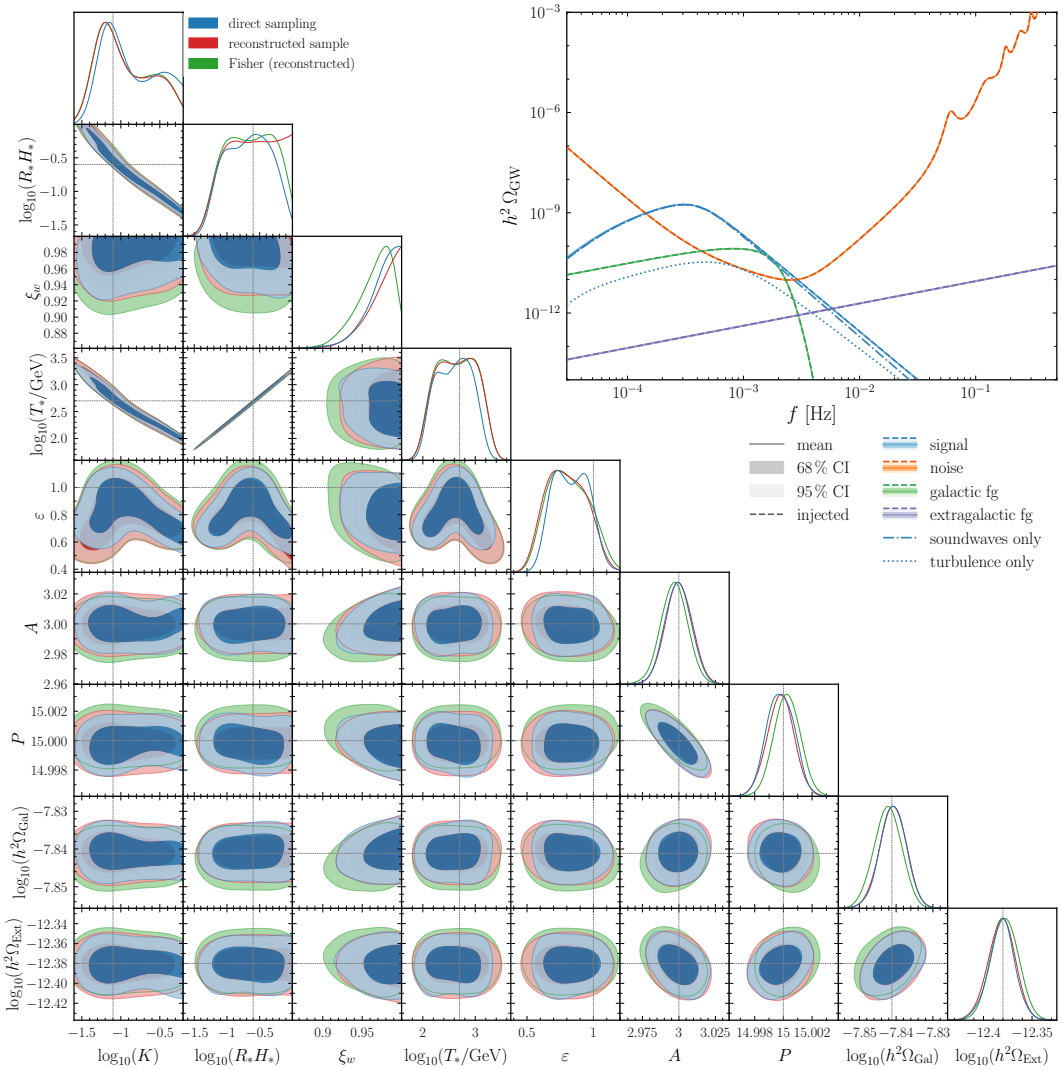

Figure 4. Taken from [15]: Template-based reconstruction of the thermodynamic parameters of a SGWB from sound waves and MHD turbulence at a moderately strong first-order PT, together with the noise and foreground parameters (note that the notation of [15] is such that $R_* = \ell_*$ and $\xi_w = v_w$). The posteriors of the direct sampling in terms of the thermodynamic parameters are shown in blue. The background red contours are reconstructed from a sample in terms of the geometric parameters of the double broken power law, and translated to the thermodynamic parameters. The green contours are obtained from a Fisher analysis in terms of the geometric parameters, also translated to the thermodynamic parameters. The inset shows the injected noise, foregrounds and signal (according to the legend), and their the reconstruction (shaded areas around the lines).

The results of [15] indicate that, under the conditions considered, it is in principle possible to infer the thermodynamic parameters from a SGWB detection by LISA, albeit with significant degeneracies. This conclusion is based on a template-based reconstruction applied to simulated data that include the SGWB signal, the instrumental

noise, and two examples of astrophysical foregrounds. It should be emphasized, however, that the simulated data are generated using the same templates for the noise, foregrounds, and SGWB that are adopted in the reconstruction. This implicitly assumes the absence of theoretical and experimental uncertainties in both the signal and noise modelling. Furthermore, in a realistic search for a SGWB in LISA data, one must contend with the intrinsic degeneracy between the signal and the instrumental noise, both of which are stochastic. Unlike ground-based interferometer networks, which can cross-correlate data streams from noise-independent detectors, and unlike PTAs, which use the Hellings-Downs angular correlation as a characteristic signature of GWs, LISA has no equivalent, unambiguous discriminator to separate a SGWB from the stationary Gaussian component of its instrumental noise. In practice, one must therefore rely on a noise model. However, it is overly optimistic to assume that a pre-flight validated noise model can be applied straightforwardly in a full data-analysis pipeline. On real data, one would first run analysis pipelines designed to jointly estimate both the noise and the SGWB signal [8–11]. Given the large variety of proposed SGWB sources, each predicting spectra with distinct features, such procedures should ideally search for a SGWB without assuming any specific template (e.g. as in [353,354]). Instead, they would attempt to infer the spectral shapes of both the SGWB and the noise directly from the measured data. Once a detection has been established through such a template-blind analysis - hopefully providing preliminary information about the spectral shape of the signal - one could then proceed to apply the template-based reconstruction approach used in Ref. [15] (see also [12,13,359–361]). At that stage, however, the analysis of real data will be further complicated by residual contamination arising from the imperfect subtraction of other GW sources in the data stream.

4.3. Connection with Two Particle Physics Scenarios

In the previous section, we highlighted the degeneracies that arise when reconstructing the thermodynamic parameters from a SGWB detection at LISA, even under the somewhat idealised working conditions of Ref. [15]. Ideally, one would even like to go a step further, and translate the reconstructed thermodynamic parameters into constraints on the parameter space of specific BSM scenarios predicting a first-order PT. However, mapping a given set of thermodynamic parameters onto the corresponding BSM model parameters is itself a highly non-linear procedure and comes with its own intrinsic degeneracies (for a through discussion and references, see [15]). These are further compounded by the degeneracies present in the reconstruction from LISA data, implying that, in general, it will not be possible to unambiguously identify the BSM model responsible for the first-order PT solely from the GW signal.

Nevertheless, it remains possible to constrain a specific BSM model once it is assumed. The fundamental parameters of the model can be mapped, in a separate step, onto the corresponding set of thermodynamic and/or geometric parameters. For each such set, one can then predict the SGWB signal. After the SGWB has been measured and the thermodynamic and/or geometric parameters have been reconstructed - together with their posterior distributions - these posteriors can be translated into the corresponding region in the parameter space of the BSM model. The LISA measurement can then be placed within a broader view of the model's parameter space and compared with the regions accessible to current and future particle-physics experiments.

This strategy was implemented in Ref. [15] for two illustrative scenarios: the Standard Model extended by a real singlet with a $\mathbb{Z}_2$ symmetry, and the Standard Model extended by a $U(1)_{B-L}$ gauge symmetry (see Section 3). These models are particularly suited as illustrative scenarios, for two reasons: they can give rise to a first-order PT with high SGWBs in the LISA frequency band, and they are characterised by few fundamental parameters. The strategy proceeds in three steps:

(1) The first step consists in predicting the GW signal within the given BSM model: one scans the allowed region in the fundamental parameter space of the model and associates to it the thermodynamic and/or geometric parameters of the signal. This procedure non trivial to implement: for detail, see [15].
(2) The second step is to simulate the LISA measurement and infer the posteriors on the geometric parameters. The latter are used in this step, rather than the thermodynamic ones, because they reduce the degeneracy in the reconstruction procedure. For this step, in practice one chooses one or more benchmark points for which the SGWB is sufficiently high in LISA.
(3) In the third step, the LISA measurement via the reconstruction of the geometric parameters can be translated into constraints on the fundamental parameter space of the BSM model, and possibly compared to pre-existing constraints or future forecasts from complementary particle physics experiments.

The results of this procedure for the $\mathbb{Z}_2$ extension of the SM, obtained in [15], are reported in Figure 5. The model is characterised by three parameters: m_s the singlet mass, λ_{hs} the portal coupling between the Higgs and the singlet, and λ_s the quartic coupling of the singlet. The strength of the PT is determined essentially by λ_{hs} which, however, cannot be too large, to remain within the perturbative regime. This in turns means that m_s

cannot be too large either: in [15], the window $65\,\mathrm{GeV} < m_s < 125\,\mathrm{GeV}$ is chosen. The upper panel of Figure 5 shows the geometric parameters (f_2, Ω_2) of the SGWB generated by sound waves from the first-order PT (double broken power law), obtained by scanning the (m_s, λ_{hs}) parameter space, for three fixed values of λ_s. To perform step 2, out of the parameter space, one particular benchmark point is chosen, featuring a SGWB high enough to be detected by LISA: in the case at hand, this corresponds to $h^2\Omega_2 = 10^{-11}$ and $f_2 = 0.4$ mHz, while the first spectral break is given by the bubble wall velocity, here set to $v_w = 1$, and the sound speed, here set to $c_s = 1/\sqrt{3}$: $f_1/f_2 \simeq 0.4|v_w - c_s|/\max(v_w, c_s)$ [15]. The outcome of the LISA parameter inference on this particular benchmark is shown in the lower left panel of Figure 5. Finally, the lower rigth panel of Figure 5 shows the posterior contours obtained from the LISA measurement translated back in the (m_s, λ_{hs}) parameter space, again for three values of λ_s: LISA can help discriminating the model parameter space, in the region that will not be probed by future colliders. This shows the complementary power of LISA in probing this particular scenario.

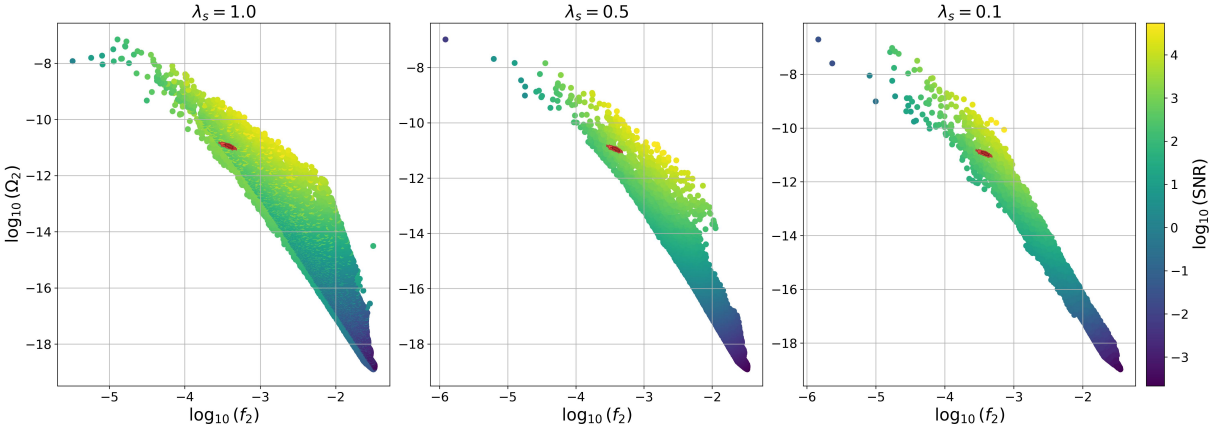

(**a**) *Step 1:* Geometric parameters (f_2, Ω_2) of the GW signal from sound waves, obtained by scanning the singlet parameter space given by the singlet mass and coupling with the Higgs (m_s, λ_{ms}), for three fixed values of the quartic coupling λ_s. The colour bar denotes the SNR in LISA of the sound waves SGWB corresponding to each (f_2, Ω_2) point. The red ellipse on top of each plot comes from the LISA measurement of the chosen benchmark point (see panel (**b**)).

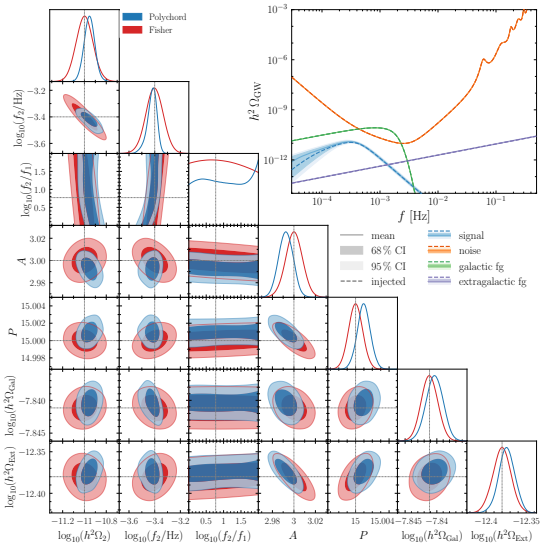

(**b**) *Step 2:* Simulated LISA measurement of the benchmark point with geometric parameters $h^2\Omega_2 = 10^{-11}$ and $f_2 = 0.4$ mHz (corresponding to the red ellipses in panel (**a**)) for the SGWB produced by sound waves (concerning f_2/f_1, see main text).

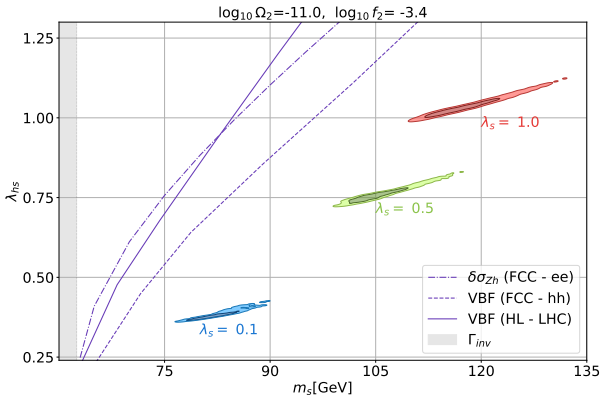

(**c**) *Step 3:* The posterior contours from the LISA measurement (c.f. panel (**b**)) shown as constraints on the fundamental parameter space of the model (m_s, λ_{ms}), for the three chosen values of the quartic coupling λ_s listed in panel (**a**). The violet curves are experimental upper limits from the FCC and the high luminosity LHC, according to the legend. The gray shaded region is excluded by Higgs invisible decay.

Figure 5. All panels taken from [15]: LISA constraints on the SM extended with a $\mathbb{Z}_2$ gauge singlet.

It is important to mention that this scenario in its simplest implementation analysed in [15] suffers from observational and theoretical challenges, linked to the overproduction of dark matter and the presence of domain walls: the latter in particular are formed in the first step of the PT, and despite being annihilated at the second step when the $\mathbb{Z}_2$ symmetry is restored, they would act as seeds for the bubble formation, altering the PT dynamics and the prediction of the GW signal [362].

The same strategy has been performed in [15] also for the case of the SM extended via the $U(1)_{B-L}$ gauge symmetry. Within this scenario the first-order PT is strong, and therefore the relevant contribution to the SGWB is given by bubbles collision, characterised by a broken power law with the two geometric parameters (f_b, Ω_b). Two different benchmark points have been chosen in [15] for step 2: $(f_b = 5\,\mathrm{mHz}, h^2\Omega_b = 4 \times 10^{-12})$, and $(f_b = 0.2\,\mathrm{Hz}, h^2\Omega_b = 6 \times 10^{-10})$. In Figure 6 we reproduce the results of step 3 in the reconstruction procedure: as expected, it appears that different measurements at LISA lead to different constraints on the model parameter space, here provided by the boson mass $m_{Z'}$ and the gauge coupling g_{B-L}.

In particular, the second benchmark point leads to a stronger degeneracy in the reconstruction of the fundamental parameters of the model, despite being characterised by a higher signal amplitude $h^2\Omega_b$ than the first benchmark point. This is because the peak of the signal is in the high-frequency region, where the LISA sensitivity is worst (c.f. plots and discussion in [15]).

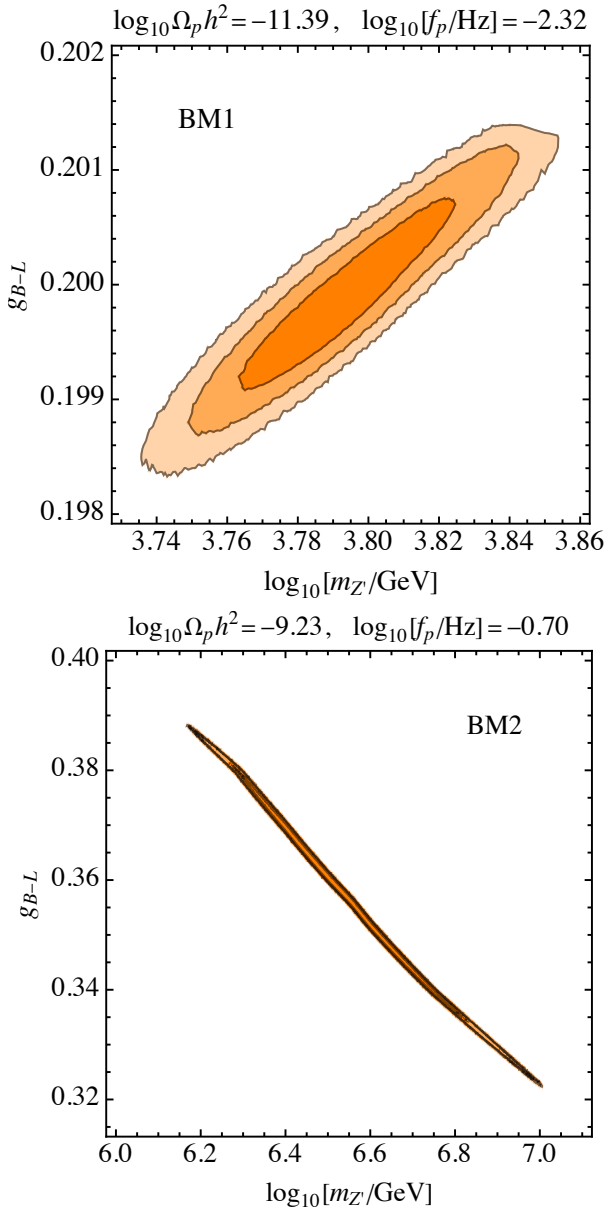

Figure 6. Taken from [15]: LISA constraints on the parameters of the SM extended with the $U(1)_{B-L}$ gauge symmetry, i.e. the gauge coupling g_{B-L} and the boson mass $m_{Z'}$, for two separate benchmark points for the parameters of the SGWB sourced by bubble collisions (f_b, Ω_b), as given in the plots' upper labels.

5. Conclusions

GWs produced in the early Universe behave as a fossil radiation: a stochastic background that can carry valuable information about high-energy physics at energy scales far beyond the reach of both cosmological probes (such as the CMB and BBN) and current particle collider experiments. Crucially, the frequency ranges of sensitivity of present and upcoming GW detectors can be associated with the energy scales of various cosmological PTs. For instance, ground-based interferometers are sensitive to energies around the Peccei–Quinn transition, LISA to the EW transition and above, and PTAs to the QCD transition.

However, detectability requires the signal amplitude to be sufficiently large. This typically demands that the PT be first-order and/or produce topological defects, which generate the anisotropic stresses sourcing GWs. A variety of BSM scenarios exist, in which the otherwise continuous transitions taking place within the SM become first-order, or in which additional symmetry-breakings occurring mainly at higher energy scales generate strong GW signals. We have provided a concise overview of several representative models of this type.

It would be extremely valuable to probe this diverse phenomenology through GW observations. We have explored this prospect in more detail focussing on the specific case of a first-order PT. We emphasized that making precise predictions for the resulting SGWB spectrum is challenging, owing to the inherently complex and highly non-linear dynamics involved, together with the large freedom available in model building and parameter choices. In general, numerical simulations are required for robust predictions and for validating analytical estimates of the signal.

In addition to the difficulty of forecasting the SGWB spectrum within a given framework, one faces the further challenge of extracting the relevant physical parameters from a potential detection. Following Ref. [15], we have focused on the case of a SGWB induced by a first-order PT and detectable by LISA. In such case, the SGWB spectrum typically exhibits fewer distinct features than the thermodynamic parameters that control it, leading to strong degeneracies in parameter reconstruction. To mitigate this issue, Ref. [15] proposes parametrising the GW signal using geometric parameters characterizing its shape, which allows for a more robust parameter reconstruction from the observed signal. However, the degeneracies re-emerge when one attempts to translate the geometric parameters back into the thermodynamic ones - an essential step in connecting a measured signal to the physics of the PT.

Ideally, one would like a LISA detection to identify which specific BSM model, among the many capable of producing a first-order PT, is responsible for a given SGWB signal. However, strong degeneracies exist also between the thermodynamic parameters of the PT and those of the underlying BSM model, making such a direct inference extremely challenging. Nevertheless, a detection - or even a non-detection - can still be used to constrain specific models, once chosen beforehand.

To do so, one must first scan the parameter space of the fundamental parameters in the chosen BSM scenario and compute the associated SGWB signal for each parameter point. The expected LISA sensitivity is then applied to simulate a detection (or exclusion), allowing one to infer confidence regions in the geometric and/or thermodynamic parameters of the first-order PT. These confidence regions can subsequently be mapped back onto the corresponding regions in the BSM model parameter space.

We presented the results of Ref. [15], where this procedure was carried out for two well-motivated BSM scenarios featuring a first-order PT. While the analysis relies on somewhat idealized assumptions and should therefore be viewed mainly as a proof of principle, it nevertheless demonstrates that LISA can provide constraints that are complementary to those expected from future particle colliders.

In conclusion, the detection of SGWBs originating from BSM processes at high energies in the early Universe holds transformative scientific potential. However, substantial progress is still required to fully realise this potential. Focusing in particular on first-order PTs, preparedness for a possible detection would ideally rely on a unified and broadly accepted theoretical framework. Achieving this goal requires progress toward consensus on several key aspects, most notably on the predicted SGWB spectra and their parameter dependencies, as well as on robust methods to connect thermodynamic parameters to the underlying high energy PT models. Establishing such a framework would ensure that the link to the fundamental theory can be reconstructed at best in a consistent, transparent, and reusable manner, facilitating community-wide adoption. This approach offers the most effective strategy for mitigating the intrinsic limitation that GW signals typically exhibit too few distinctive features to unambiguously discriminate among the different underlying scenarios.

Data Availability Statement

Not applicable.

Acknowledgments

The author acknowledges informative discussions with Germano Nardini.

Conflicts of Interest

The author declares no conflict of interest.

Use of AI and AI-Assisted Technologies

During the preparation of this work, the author used ChatGPT to correct the English when in doubt. After using this tool, the author reviewed and edited the content as needed and takes full responsibility for the content of the published article.

Appendix A. Summary Table of the Key Parameters

Table A1. Summary table of the key parameters.

Parameter	Meaning
ℓ_* (R_*)	characteristic length scale of the GW sourcing process (i.e. bubble size in the case of a first-orde PT)
T_*	temperature of the early Universe when the GW sourcing process was operating
$\Pi/\rho^*_{\rm tot}$	anisotropic stresses available to source the GWs, normalised to the energy density in the Universe at the source time
v_w (ξ_w)	bubble wall velocity
β	PT rate parameter
t_*	reference time corresponding to T_*
$K=\rho_s/\rho^*_{\rm tot}$	GW source energy fraction
ρ_φ	gradient energy in the scalar field
ρ_v	kinetic energy of the bulk fluid motion
$\kappa_{\varphi,v}=\rho_{\varphi,v}/\Delta V_0$	efficiency parameters (efficiency with which the potential energy is transformed into gradient energy of the bubble walls or kinetic energy of the fluid)
$\alpha=\Delta V_0/[\pi^2 g(T_*)T_*^4/30]$	strength of the PT (fraction of the potential to thermal energy)
$\tilde{\Omega}_{\rm GW}$	efficiency with which the GW source energy fraction K is converted to GWs
$S(f)$	normalised SGWB spectral shape
ϵ	fraction of kinetic energy in bulk motion that is converted to (MHD) turbulence
f_b, Ω_b	geometric parameters of the broken power law template: frequency of, and amplitude at, the spectral peak
f_1, f_2, Ω_2	geometric parameters of the double broken power law template: frequencies of the two breaks and amplitude at the second break
A, P	parameters of the LISA noise: amplitudes of the acceleration and test mass noises
$h^2\Omega_{\rm Gal}$	amplitude of the Galactic foreground in LISA
$h^2\Omega_{\rm Ext}$	amplitude of the extra-Galactic foreground in LISA
m_s	singlet mass in the $\mathbb{Z}_2$ extension of the SM
λ_{hs}	portal coupling between the Higgs and the singlet
λ_s	quartic coupling of the singlet
$m_{Z'}$	boson mass in the SM extended by $U(1)_{B-L}$ gauge symmetry
g_{B-L}	boson gauge coupling

References

1. Maggiore, M. Gravitational wave experiments and early universe cosmology. *Phys. Rep.* **2000**, *331*, 283–367.
2. Durrer, R. *The Cosmic Microwave Background*; Cambridge University Press: Cambridge, UK, 2020.
3. Caprini, C.; Figueroa, D.G. Cosmological Backgrounds of Gravitational Waves. *Class. Quant. Grav.* **2018**, *35*, 163001.
4. Maggiore, M. *Gravitational Waves: Astrophysics and Cosmology*; Oxford University Press: Oxford, UK, 2018; Volume 2.
5. Athron, P.; Balázs, C.; Fowlie, A.; et al. Cosmological phase transitions: From perturbative particle physics to gravitational waves. *Prog. Part. Nucl. Phys.* **2024**, *135*, 104094.
6. Romano, J.D.; Cornish, N.J. Detection methods for stochastic gravitational-wave backgrounds: A unified treatment. *Living Rev. Rel.* **2017**, *20*, 2.
7. Colpi, M.; Danzmann, K.; Hewitson, M.; et al. LISA Definition Study Report. *arXiv* **2024**, arXiv:2402.07571.

8. Baghi, Q.; Karnesis, N.; Bayle, J.B.; et al. Uncovering gravitational-wave backgrounds from noises of unknown shape with LISA. *J. Cosmol. Astropart. Phys.* **2023**, *2023*, 066.
9. Karnesis, N.; Lilley, M.; Petiteau, A. Assessing the detectability of a Stochastic Gravitational Wave Background with LISA, using an excess of power approach. *Class. Quant. Grav.* **2020**, *37*, 215017.
10. Santini, A.; Muratore, M.; Gair, J.; et al. Flexible, GPU-accelerated approach for the joint characterization of LISA instrumental noise and stochastic gravitational wave backgrounds. *Phys. Rev. D* **2025**, *112*, 084050.
11. Pozzoli, F.; Gair, J.; Buscicchio, R.; et al. Is the stochastic signal really detectable? *Phys. Rev. D* **2025**, *112*, 064035.
12. Boileau, G.; Christensen, N.; Gowling, C.; et al. Prospects for LISA to detect a gravitational-wave background from first order phase transitions. *J. Cosmol. Astropart. Phys.* **2023**, *02*, 056.
13. Hindmarsh, M.; Hooper, D.C.; Minkkinen, T.; et al. Recovering a phase transition signal in simulated LISA data with a modulated galactic foreground. *J. Cosmol. Astropart. Phys.* **2025**, *2025*, 052.
14. Caprini, C.; Pujolàs, O.; Quelquejay-Leclere, H.; et al. Primordial gravitational wave backgrounds from phase transitions with next generation ground based detectors. *Class. Quant. Grav.* **2025**, *42*, 045015.
15. Caprini, C.; Jinno, R.; Lewicki, M.; et al. Gravitational waves from first-order phase transitions in LISA: reconstruction pipeline and physics interpretation. *J. Cosmol. Astropart. Phys.* **2024**, *2024*, 020.
16. Bartolo, N.; Bertacca, D.; Caldwell, R.; et al. Probing anisotropies of the Stochastic Gravitational Wave Background with LISA. *J. Cosmol. Astropart. Phys.* **2022**, *2022*, 009.
17. Available online: https://www.ligo.caltech.edu/ (accessed on 10 November 2025).
18. Available online: https://www.virgo-gw.eu/ (accessed on 10 November 2025).
19. Available online: https://gwcenter.icrr.u-tokyo.ac.jp/en/ (accessed on 10 November 2025).
20. Peccei, R.D.; Quinn, H.R. CP Conservation in the Presence of Instantons. *Phys. Rev. Lett.* **1977**, *38*, 1440–1443.
21. Peccei, R.D.; Quinn, H.R. Constraints Imposed by CP Conservation in the Presence of Instantons. *Phys. Rev. D* **1977**, *16*, 1791–1797.
22. Kim, J.E. Weak Interaction Singlet and Strong CP Invariance. *Phys. Rev. Lett.* **1979**, *43*, 103.
23. Shifman, M.A.; Vainshtein, A.I.; Zakharov, V.I. Can Confinement Ensure Natural CP Invariance of Strong Interactions? *Nucl. Phys. B* **1980**, *166*, 493–506.
24. Dine, M.; Fischler, W.; Srednicki, M. A Simple Solution to the Strong CP Problem with a Harmless Axion. *Phys. Lett. B* **1981**, *104*, 199–202.
25. Zhitnitsky, A.R. On Possible Suppression of the Axion Hadron Interactions. *Sov. J. Nucl. Phys.* **1980**, *31*, 260. (In Russian)
26. Raffelt, G.G. Astrophysical methods to constrain axions and other novel particle phenomena. *Phys. Rep.* **1990**, *198*, 1–113.
27. Miller Bertolami, M.M.; Melendez, B.E.; Althaus, L.G.; et al. Revisiting the axion bounds from the Galactic white dwarf luminosity function. *J. Cosmol. Astropart. Phys.* **2014**, *10*, 069.
28. Ayala, A.; Domínguez, I.; Giannotti, M.; et al. Revisiting the bound on axion-photon coupling from Globular Clusters. *Phys. Rev. Lett.* **2014**, *113*, 191302.
29. Dolan, M.J.; Hiskens, F.J.; Volkas, R.R. Advancing globular cluster constraints on the axion-photon coupling. *J. Cosmol. Astropart. Phys.* **2022**, *10*, 096.
30. Bar, N.; Blum, K.; D'Amico, G. Is there a supernova bound on axions? *Phys. Rev. D* **2020**, *101*, 123025.
31. Chang, J.H.; Essig, R.; McDermott, S.D. Supernova 1987A Constraints on Sub-GeV Dark Sectors, Millicharged Particles, the QCD Axion, and an Axion-like Particle. *J. High Energy Phys.* **2018**, *2018*, 51.
32. Carenza, P.; Fore, B.; Giannotti, M.; et al. Enhanced Supernova Axion Emission and its Implications. *Phys. Rev. Lett.* **2021**, *126*, 071102.
33. Notari, A.; Rompineve, F.; Villadoro, G. Improved Hot Dark Matter Bound on the QCD Axion. *Phys. Rev. Lett.* **2023**, *131*, 011004.
34. Gorghetto, M.; Hardy, E.; Villadoro, G. Axions from Strings: The Attractive Solution. *J. High Energy Phys.* **2018**, *2018*, 151.
35. Gorghetto, M.; Hardy, E.; Villadoro, G. More axions from strings. *SciPost Phys.* **2021**, *10*, 050.
36. Buschmann, M.; Foster, J.W.; Hook, A.; et al. Dark matter from axion strings with adaptive mesh refinement. *Nat. Commun.* **2022**, *13*, 1049.
37. Saikawa, K.; Redondo, J.; Vaquero, A.; et al. Spectrum of global string networks and the axion dark matter mass. *J. Cosmol. Astropart. Phys.* **2024**, *10*, 043.
38. Abac, A.G.; Abouelfettouh, I.; Acernese, F.; et al. Upper Limits on the Isotropic Gravitational-Wave Background from the first part of LIGO, Virgo, and KAGRA's fourth Observing Run. *arXiv* **2025**, arXiv:2508.20721.
39. Abac, A.G.; Abouelfettouh, I.; Acernese, F.; et al. Cosmological and High Energy Physics implications from gravitational-wave background searches in LIGO-Virgo-KAGRA's O1-O4a runs. *arXiv* **2025**, arXiv:2510.26848.
40. Available online: https://www.et-gw.eu/ (accessed on 10 November 2025).
41. Available online: https://cosmicexplorer.org/ (accessed on 10 November 2025).
42. Maggiore, M.; Iacovelli, F.; Belgacem, E.; et al. Comparison of global networks of third-generation gravitational-wave detectors. *Class. Quant. Grav.* **2025**, *42*, 215004.

43. Branchesi, M.; Maggiore, M.; Alonso, D.; et al. Science with the Einstein Telescope: A comparison of different designs. *J. Cosmol. Astropart. Phys.* **2023**, *2023*, 068.
44. Bellie, D.S.; Banagiri, S.; Doctor, Z.; et al. The unresolved stochastic background from compact binary mergers detectable by next-generation ground-based gravitational-wave observatories. *Phys. Rev. D* **2024**, *110*, 023006.
45. Zhou, B.; Reali, L.; Berti, E.; et al. Compact Binary Foreground Subtraction in Next-Generation Ground-Based Observatories. *arXiv* **2022**, arXiv:2209.01221.
46. Zhou, B.; Reali, L.; Berti, E.; et al. Subtracting compact binary foregrounds to search for subdominant gravitational-wave backgrounds in next-generation ground-based observatories. *Phys. Rev. D* **2023**, *108*, 064040.
47. Abac, A.; Abramo, R.; Albanesi, S.; et al. The Science of the Einstein Telescope. *arXiv* **2025**, arXiv:2503.12263.
48. Von Harling, B.; Pomarol, A.; Pujolàs, O.; et al. Peccei-Quinn Phase Transition at LIGO. *J. High Energy Phys.* **2020**, *2020*, 195.
49. Zambujal Ferreira, R.; Notari, A.; Pujolàs, O.; et al. High Quality QCD Axion at Gravitational Wave Observatories. *Phys. Rev. Lett.* **2022**, *128*, 141101.
50. Available online: https://www.esa.int/Science_Exploration/Space_Science/LISA (accessed on 10 November 2025).
51. Binetruy, P.; Bohe, A.; Caprini, C.; et al. Cosmological Backgrounds of Gravitational Waves and eLISA/NGO: Phase Transitions, Cosmic Strings and Other Sources. *J. Cosmol. Astropart. Phys.* **2012**, *2012*, 027.
52. Caprini, C.; Hindmarsh, M.; Huber, S.; et al. Science with the space-based interferometer eLISA. II: Gravitational waves from cosmological phase transitions. *J. Cosmol. Astropart. Phys.* **2016**, *2016*, 001.
53. Caprini, C.; Chala, M.; Dorsch, G.C.; et al. Detecting gravitational waves from cosmological phase transitions with LISA: An update. *J. Cosmol. Astropart. Phys.* **2020**, *2020*, 024.
54. Farmer, A.J.; Phinney, E.S. The gravitational wave background from cosmological compact binaries. *Mon. Not. Roy. Astron. Soc.* **2003**, *346*, 1197.
55. Lamberts, A.; Blunt, S.; Littenberg, T.B.; et al. Predicting the LISA white dwarf binary population in the Milky Way with cosmological simulations. *Mon. Not. Roy. Astron. Soc.* **2019**, *490*, 5888–5903.
56. Staelens, S.; Nelemans, G. Likelihood of white dwarf binaries to dominate the astrophysical gravitational wave background in the mHz band. *Astron. Astrophys.* **2024**, *683*, A139.
57. Korol, V.; Hallakoun, N.; Toonen, S.; et al. Observationally driven Galactic double white dwarf population for LISA. *Mon. Not. Roy. Astron. Soc.* **2022**, *511*, 5936–5947.
58. Karnesis, N.; Babak, S.; Pieroni, M.; et al. Characterization of the stochastic signal originating from compact binary populations as measured by LISA. *Phys. Rev. D* **2021**, *104*, 043019.
59. Babak, S.; Caprini, C.; Figueroa, D.G.; et al. Stochastic gravitational wave background from stellar origin binary black holes in LISA. *J. Cosmol. Astropart. Phys.* **2023**, *2023*, 034.
60. Lehoucq, L.; Dvorkin, I.; Srinivasan, R.; et al. Astrophysical uncertainties in the gravitational-wave background from stellar-mass compact binary mergers. *Mon. Not. Roy. Astron. Soc.* **2023**, *526*, 4378–4387.
61. Piarulli, M.; Buscicchio, R.; Pozzoli, F.; et al. Test for LISA foreground Gaussianity and stationarity: Extreme mass-ratio inspirals. *Phys. Rev. D* **2025**, *111*, 103047.
62. Antoniadis, J.; Arumugam, P.; Arumugam, S.; et al. The second data release from the European Pulsar Timing Array—III. Search for gravitational wave signals. *Astron. Astrophys.* **2023**, *678*, A50.
63. Agazie, G.; Anumarlapudi, A.; Archibald, A.M.; et al. The NANOGrav 15 yr Data Set: Evidence for a Gravitational-wave Background. *Astrophys. J. Lett.* **2023**, *951*, L8.
64. Reardon, D.J.; Zic, A.; Shannon, R.M.; et al. Search for an Isotropic Gravitational-wave Background with the Parkes Pulsar Timing Array. *Astrophys. J. Lett.* **2023**, *951*, L6.
65. Xu, H.; Chen, S.; Guo, Y.; et al. Searching for the Nano-Hertz Stochastic Gravitational Wave Background with the Chinese Pulsar Timing Array Data Release I. *Res. Astron. Astrophys.* **2023**, *23*, 075024.
66. Antoniadis, J.; Arzoumanian, Z.; Babak, S.; et al. The International Pulsar Timing Array second data release: Search for an isotropic gravitational wave background. *Mon. Not. Roy. Astron. Soc.* **2022**, *510*, 4873–4887.
67. Rawlings, S.; Schilizzi, R. The Square Kilometre Array. *arXiv* **2011**, arXiv:1105.5953.
68. Janssen, G.; Hobbs, G.; McLaughlin, M.; et al. Gravitational wave astronomy with the SKA. *Proc. Sci.* **2015**, *AASKA14*, 037.
69. Antoniadis, J.; Arumugam, P.; Arumugam, S.; et al. The second data release from the European Pulsar Timing Array: V. Implications for massive black holes, dark matter and the early Universe. *Astron. Astrophys.* **2023**, *685*, A94.
70. Agazie, G.; Anumarlapudi, A.; Archibald, A.M.; et al. The NANOGrav 15 yr Data Set: Constraints on Supermassive Black Hole Binaries from the Gravitational-wave Background. *Astrophys. J. Lett.* **2023**, *952*, L37.
71. Figueroa, D.G.; Pieroni, M.; Ricciardone, A.; et al. Cosmological Background Interpretation of Pulsar Timing Array Data. *Phys. Rev. Lett.* **2024**, *132*, 171002.
72. Ellis, J.; Fairbairn, M.; Franciolini, G.; et al. What is the source of the PTA GW signal? *Phys. Rev. D* **2024**, *109*, 023522.
73. Afzal, A.; Agazie, G.; Anumarlapudi, A.; et al. The NANOGrav 15 yr Data Set: Search for Signals from New Physics. *Astrophys. J. Lett.* **2023**, *951*, L11.
74. Caprini, C.; Durrer, R.; Siemens, X. Detection of gravitational waves from the QCD phase transition with pulsar timing arrays. *Phys. Rev. D* **2010**, *82*, 063511.

75. Neronov, A.; Roper Pol, A.; Caprini, C.; et al. NANOGrav signal from magnetohydrodynamic turbulence at the QCD phase transition in the early Universe. *Phys. Rev. D* **2021**, *103*, 041302.
76. Roper Pol, A.; Caprini, C.; Neronov, A.; et al. Gravitational wave signal from primordial magnetic fields in the Pulsar Timing Array frequency band. *Phys. Rev. D* **2022**, *105*, 123502.
77. Cline, J.M.; Laurent, B. Bubble wall velocity for first-order QCD phase transition. *Phys. Rev. D* **2025**, *111*, 083522.
78. Zheng, H.W.; Gao, F.; Bian, L.; et al. Quantitative analysis of the gravitational wave spectrum sourced from a first-order chiral phase transition of QCD. *Phys. Rev. D* **2025**, *111*, L021303.
79. Sedda, M.A.; Berry, C.P.; Jani, K.; et al. The missing link in gravitational-wave astronomy: Discoveries waiting in the decihertz range. *Class. Quant. Grav.* **2020**, *37*, 215011.
80. Perego, A.; Bonetti, M.; Sesana, A.; et al. Assessing the performance of future space-based detectors: astrophysical foregrounds and individual sources. *arXiv* **2025**, arXiv:2510.18695.
81. El-Neaj, Y.A.; Alpigiani, C.; Amairi-Pyka, S.; et al. AEDGE: Atomic Experiment for Dark Matter and Gravity Exploration in Space. *EPJ Quant. Technol.* **2020**, *7*, 6.
82. Badurina, L.; Bentine, E.; Blas, D.; et al. AION: An Atom Interferometer Observatory and Network. *J. Cosmol. Astropart. Phys.* **2020**, *2020*, 011.
83. Baynham, C.F.A.; Hobson, R.; Buchmueller, O.; et al. A Prototype Atom Interferometer to Detect Dark Matter and Gravitational Waves. *arXiv* **2025**, arXiv:2504.09158.
84. Abend, S.; Allard, B.; Alonso, I.; et al. Terrestrial Very-Long-Baseline Atom Interferometry: Workshop Summary. *AVS Quantum Sci.* **2024**, *6*, 02470.
85. Abdalla, A.; Abe, M.; Abend, S.; et al. Terrestrial Very-Long-Baseline Atom Interferometry: Summary of the second workshop. *EPJ Quant. Technol.* **2025**, *12*, 42.
86. Ajith, P.; Seoane, P.A.; Sedda, M.A.; et al. The Lunar Gravitational-wave Antenna: Mission studies and science case. *arXiv* **2025**, arXiv:2509.25952.
87. Jani, K.; Abernathy, M.; Berti, E.; et al. Laser Interferometer Lunar Antenna (LILA): Advancing the U.S. Priorities in Gravitational-wave and Lunar Science. *arXiv* **2025**, arXiv:2508.11631.
88. Book, L.G.; Flanagan, E.E. Astrometric Effects of a Stochastic Gravitational Wave Background. *Phys. Rev. D* **2011**, *83*, 024024.
89. Mihaylov, D.P.; Moore, C.J.; et al. Astrometric Effects of Gravitational Wave Backgrounds with non-Einsteinian Polarizations. *Phys. Rev. D* **2018**, *97*, 124058.
90. Moore, C.J.; Mihaylov, D.P.; Lasenby, A.; et al. Astrometric Search Method for Individually Resolvable Gravitational Wave Sources with Gaia. *Phys. Rev. Lett.* **2017**, *119*, 261102.
91. Crosta, M.; Lattanzi, M.G.; Le Poncin-Lafitte, C.; et al. Pinpointing gravitational waves via astrometric gravitational wave antennas. *Sci. Rep.* **2024**, *14*, 5074.
92. Klioner, S.A. Gaia-like astrometry and gravitational waves. *Class. Quant. Grav.* **2018**, *35*, 045005.
93. Darling, J.; Truebenbach, A.E.; Paine, J. Astrometric Limits on the Stochastic Gravitational Wave Background. *Astrophys. J.* **2018**, *861*, 113.
94. Garcia-Bellido, J.; Murayama, H.; White, G. Exploring the early Universe with Gaia and Theia. *J. Cosmol. Astropart. Phys.* **2021**, *12*, 023.
95. Aggarwal, N.; Aguiar, O.D.; Bauswein, A.; et al. Challenges and opportunities of gravitational-wave searches at MHz to GHz frequencies. *Living Rev. Rel.* **2021**, *24*, 4.
96. Aggarwal, N.; Aguiar, O.D.; Blas, D.; et al. Challenges and Opportunities of Gravitational Wave Searches above 10 kHz. *arXiv* **2025**, arXiv:2501.11723.
97. Domcke, V.; Ellis, S.A.R.; Kopp, J. Dielectric haloscopes as gravitational wave detectors. *Phys. Rev. D* **2025**, *111*, 035031.
98. Berlin, A.; Blas, D.; Tito D'Agnolo, R.; et al. Electromagnetic cavities as mechanical bars for gravitational waves. *Phys. Rev. D* **2023**, *108*, 084058.
99. Domcke, V.; Garcia-Cely, C.; Rodd, N.L. Novel Search for High-Frequency Gravitational Waves with Low-Mass Axion Haloscopes. *Phys. Rev. Lett.* **2022**, *129*, 041101.
100. Aghanim, N.; Akrami, Y.; Ashdown, M.; et al. Planck 2018 results. VI. Cosmological parameters. *Astron. Astrophys.* **2020**, *641*, A6.
101. Caldwell, R.; Cui, Y.; Guo, H.K.; et al. Detection of early-universe gravitational-wave signatures and fundamental physics. *Gen. Rel. Grav.* **2022**, *54*, 156.
102. Roshan, R.; White, G. Using gravitational waves to see the first second of the Universe. *Rev. Mod. Phys.* **2024**, *97*, 015001.
103. Vilenkin, A.; Shellard, E.P.S. *Cosmic Strings and Other Topological Defects*; Cambridge University Press: Cambridge, UK, 2000.
104. Hindmarsh, M.B.; Kibble, T.W.B. Cosmic Strings. *Rep. Prog. Phys.* **1995**, *58*, 477–562.
105. Vachaspati, T.; Pogosian, L.; Steer, D. Cosmic Strings. *Scholarpedia* **2015**, *10*, 31682.
106. Kosowsky, A.; Turner, M.S.; Watkins, R. Gravitational radiation from colliding vacuum bubbles. *Phys. Rev. D* **1992**, *45*, 4514–4535.

107. Kosowsky, A.; Turner, M.S. Gravitational radiation from colliding vacuum bubbles: Envelope approximation to many bubble collisions. *Phys. Rev. D* **1993**, *47*, 4372–4391.
108. Huber, S.J.; Konstandin, T. Gravitational Wave Production by Collisions: More Bubbles. *J. Cosmol. Astropart. Phys.* **2008**, *2008*, 22.
109. Cutting, D.; Hindmarsh, M.; Weir, D.J. Gravitational waves from vacuum first-order phase transitions: From the envelope to the lattice. *Phys. Rev. D* **2018**, *97*, 123513.
110. Cutting, D.; Escartin, E.G.; Hindmarsh, M.; et al. Gravitational waves from vacuum first order phase transitions II: from thin to thick walls. *Phys. Rev. D* **2021**, *103*, 023531.
111. Caprini, C.; Durrer, R.; Servant, G. Gravitational wave generation from bubble collisions in first-order phase transitions: An analytic approach. *Phys. Rev. D* **2008**, *77*, 124015.
112. Jinno, R.; Takimoto, M. Gravitational waves from bubble collisions: An analytic derivation. *Phys. Rev. D* **2017**, *95*, 024009.
113. Kamionkowski, M.; Kosowsky, A.; Turner, M.S. Gravitational radiation from first order phase transitions. *Phys. Rev. D* **1994**, *49*, 2837–2851.
114. Espinosa, J.R.; Konstandin, T.; No, J.M.; et al. Energy Budget of Cosmological First-order Phase Transitions. *J. Cosmol. Astropart. Phys.* **2010**, *2010*, 028.
115. Konstandin, T. Gravitational radiation from a bulk flow model. *J. Cosmol. Astropart. Phys.* **2018**, *2018*, 047.
116. Ellis, J.; Lewicki, M.; No, J.M.; et al. Gravitational wave energy budget in strongly supercooled phase transitions. *J. Cosmol. Astropart. Phys.* **2019**, *1906*, 024.
117. Lewicki, M.; Vaskonen, V. Gravitational waves from bubble collisions and fluid motion in strongly supercooled phase transitions. *Eur. Phys. J. C* **2023**, *83*, 109.
118. Hogan, C.J. Gravitational radiation from cosmological phase transitions. *Mon. Not. Roy. Astron. Soc.* **1986**, *218*, 629–636.
119. Hindmarsh, M.; Huber, S.J.; Rummukainen, K.; et al. Numerical simulations of acoustically generated gravitational waves at a first order phase transition. *Phys. Rev. D* **2015**, *92*, 123009.
120. Hindmarsh, M.; Huber, S.J.; Rummukainen, K.; et al. Shape of the acoustic gravitational wave power spectrum from a first order phase transition. *Phys. Rev. D* **2017**, *96*, 103520.
121. Cutting, D.; Hindmarsh, M.; Weir, D.J. Vorticity, kinetic energy, and suppressed gravitational wave production in strong first order phase transitions. *Phys. Rev. Lett.* **2020**, *125*, 021302.
122. Hindmarsh, M.; Hijazi, M. Gravitational waves from first order cosmological phase transitions in the Sound Shell Model. *J. Cosmol. Astropart. Phys.* **2019**, *12*, 062.
123. Dolgov, A.D.; Grasso, D.; Nicolis, A. Relic backgrounds of gravitational waves from cosmic turbulence. *Phys. Rev. D* **2002**, *66*, 103505.
124. Caprini, C.; Durrer, R. Gravitational waves from stochastic relativistic sources: Primordial turbulence and magnetic fields. *Phys. Rev. D* **2006**, *74*, 063521.
125. Gogoberidze, G.; Kahniashvili, T.; Kosowsky, A. The Spectrum of Gravitational Radiation from Primordial Turbulence. *Phys. Rev. D* **2007**, *76*, 083002.
126. Kahniashvili, T.; Campanelli, L.; Gogoberidze, G.; et al. Gravitational Radiation from Primordial Helical Inverse Cascade MHD Turbulence. *Phys. Rev. D* **2008**, *78*, 123006. Erratum in *Phys. Rev. D* **2009**, *79*, 109901.
127. Caprini, C.; Durrer, R.; Servant, G. The stochastic gravitational wave background from turbulence and magnetic fields generated by a first-order phase transition. *J. Cosmol. Astropart. Phys.* **2009**, *12*, 024.
128. Brandenburg, A.; Kahniashvili, T.; Mandal, S.; et al. Evolution of hydromagnetic turbulence from the electroweak phase transition. *Phys. Rev. D* **2017**, *96*, 123528.
129. Niksa, P.; Schlederer, M.; Sigl, G. Gravitational Waves produced by Compressible MHD Turbulence from Cosmological Phase Transitions. *Class. Quantum Gravity* **2018**, *35*, 144001.
130. Roper Pol, A.; Mandal, S.; Brandenburg, A.; et al. Numerical simulations of gravitational waves from early-universe turbulence. *Phys. Rev. D* **2020**, *102*, 083512.
131. Auclair, P.; Caprini, C.; Cutting, D.; et al. Generation of gravitational waves from freely decaying turbulence. *J. Cosmol. Astropart. Phys.* **2022**, *2022*, 29.
132. Caprini, C.; Durrer, R. Gravitational wave production: A Strong constraint on primordial magnetic fields. *Phys. Rev. D* **2001**, *65*, 023517.
133. Caprini, C.; Durrer, R.; Fenu, E. Can the observed large scale magnetic fields be seeded by helical primordial fields? *J. Cosmol. Astropart. Phys.* **2009**, *11*, 001.
134. Kahniashvili, T.; Gogoberidze, G.; Ratra, B. Gravitational Radiation from Primordial Helical MHD Turbulence. *Phys. Rev. Lett.* **2008**, *100*, 231301.
135. Kahniashvili, T.; Kisslinger, L.; Stevens, T. Gravitational Radiation Generated by Magnetic Fields in Cosmological Phase Transitions. *Phys. Rev. D* **2010**, *81*, 023004.
136. Durrer, R.; Neronov, A. Cosmological Magnetic Fields: Their Generation, Evolution and Observation. *Astron. Astrophys. Rev.* **2013**, *21*, 62.
137. Baym, G.; Bodeker, D.; McLerran, L.D. Magnetic fields produced by phase transition bubbles in the electroweak phase transition. *Phys. Rev. D* **1996**, *53*, 662–667.

138. Cheng, B.l.; Olinto, A.V. Primordial magnetic fields generated in the quark—hadron transition. *Phys. Rev. D* **1994**, *50*, 2421–2424.
139. Sigl, G.; Olinto, A.V.; Jedamzik, K. Primordial magnetic fields from cosmological first order phase transitions. *Phys. Rev. D* **1997**, *55*, 4582–4590.
140. Giudice, G.F.; Lee, H.M.; Pomarol, A.; et al. Nonthermal Heavy Dark Matter from a First-Order Phase Transition. *arXiv* **2024**, arXiv:hep-ph/2403.03252.
141. Cataldi, M.; Shakya, B. Leptogenesis via Bubble Collisions. *arXiv* **2024**, arXiv:hep-ph/2407.16747.
142. Jinno, R.; Shakya, B.; van de Vis, J. Gravitational Waves from Feebly Interacting Particles in a First Order Phase Transition. *arXiv* **2022**, arXiv:gr-qc/2211.06405.
143. Inomata, K.; Kamionkowski, M.; Kasai, K.; et al. Gravitational waves from particles produced from bubble collisions in first-order phase transitions. *Phys. Rev. D* **2025**, *112*, 083523.
144. Durrer, R.; Kunz, M.; Melchiorri, A. Cosmic structure formation with topological defects. *Phys. Rep.* **2002**, *364*, 1–81.
145. Figueroa, D.G.; Hindmarsh, M.; Urrestilla, J. Exact Scale-Invariant Background of Gravitational Waves from Cosmic Defects. *Phys. Rev. Lett.* **2013**, *110*, 101302.
146. Auclair, P.; Blanco-Pillado, J.J.; Figueroa, D.G.; et al. Probing the gravitational wave background from cosmic strings with LISA. *J. Cosmol. Astropart. Phys.* **2020**, *2020*, 034.
147. Simakachorn, P. Charting Cosmological History and New Particle Physics with Primordial Gravitational Waves. Ph.D. Thesis, Universität Hamburg, Hamburg, Germany, 2022.
148. Kibble, T.W.B. Topology of Cosmic Domains and Strings. *J. Phys. A* **1976**, *9*, 1387–1398.
149. Durrer, R. Topological defects in cosmology. *New Astron. Rev.* **1999**, *43*, 111–156.
150. Saikawa, K. A review of gravitational waves from cosmic domain walls. *Universe* **2017**, *3*, 40.
151. Damour, T.; Vilenkin, A. Gravitational wave bursts from cosmic strings. *Phys. Rev. Lett.* **2000**, *85*, 3761–3764.
152. Damour, T.; Vilenkin, A. Gravitational wave bursts from cusps and kinks on cosmic strings. *Phys. Rev. D* **2001**, *64*, 064008.
153. Binetruy, P.; Bohe, A.; Hertog, T.; et al. Gravitational Wave Bursts from Cosmic Superstrings with Y-junctions. *Phys. Rev. D* **2009**, *80*, 123510.
154. Kalb, M.; Ramond, P. Classical direct interstring action. *Phys. Rev. D* **1974**, *9*, 2273–2284.
155. Davis, R.; Shellard, E. Antisymmetric tensors and spontaneous symmetry breaking. *Phys. Lett. B* **1988**, *214*, 219–222.
156. Harari, D.; Sikivie, P. On the evolution of global strings in the early universe. *Phys. Lett. B* **1987**, *195*, 361–365.
157. Davis, R.L. Goldstone bosons in string models of galaxy formation. *Phys. Rev. D* **1985**, *32*, 3172–3177.
158. Battye, R.A.; Shellard, E.P.S. Recent perspectives on axion cosmology. *arXiv* **1997**, arXiv:astro-ph/9706014.
159. Brandenberger, R.H. On the Decay of Cosmic String Loops. *Nucl. Phys.* **1987**, *B293*, 812–828.
160. Vachaspati, T. Cosmic Rays from Cosmic Strings with Condensates. *Phys. Rev.* **2010**, *D81*, 043531.
161. Long, A.J.; Hyde, J.M.; Vachaspati, T. Cosmic Strings in Hidden Sectors: 1. Radiation of Standard Model Particles. *J. Cosmol. Astropart. Phys.* **2014**, *1409*, 030.
162. MacGibbon, J.H.; Brandenberger, R.H. High-energy neutrino flux from ordinary cosmic strings. *Nucl. Phys. B* **1990**, *331*, 153–172.
163. Steer, D.A.; Vachaspati, T. Light from Cosmic Strings. *Phys. Rev. D* **2011**, *83*, 043528.
164. Vachaspati, T. *Kinks and Domain Walls: An Introduction to Classical and Quantum Solitons*; Cambridge University Press: Cambridge, UK, 2010.
165. Kitajima, N.; Lee, J.; Murai, K.; et al. Gravitational Waves from Domain Wall Collapse, and Application to Nanohertz Signals with QCD-coupled Axions. *arXiv* **2023**, arXiv:hep-ph/2306.17146.
166. Ferreira, R.Z.; Notari, A.; Pujolàs, O.; et al. Collapsing Domain Wall Networks: Impact on Pulsar Timing Arrays and Primordial Black Holes. *arXiv* **2024**, arXiv:astro-ph.CO/2401.14331.
167. Ade, P.A.R.; Aghanim, N.; Armitage-Caplan, C.; et al. Planck 2013 results. XXV. Searches for cosmic strings and other topological defects. *Astron. Astrophys.* **2014**, *571*, A25.
168. Ringeval, C. Cosmic strings and their induced non-Gaussianities in the cosmic microwave background. *Adv. Astron.* **2010**, *2010*, 380507.
169. Aoki, Y.; Endrodi, G.; Fodor, Z.; et al. The Order of the quantum chromodynamics transition predicted by the standard model of particle physics. *Nature* **2006**, *443*, 675–678.
170. Stephanov, M.A. QCD phase diagram: An Overview. *PoS* **2006**, *LAT2006*, 024.
171. Gurtler, M.; Ilgenfritz, E.M.; Schiller, A. Where the electroweak phase transition ends. *Phys. Rev. D* **1997**, *56*, 3888–3895.
172. Aoki, Y. Four-dimensional simulation of the hot electroweak phase transition with the SU(2) gauge Higgs model. *Phys. Rev. D* **1997**, *56*, 3860–3865.
173. Kajantie, K.; Laine, M.; Rummukainen, K.; et al. The Electroweak phase transition: A Nonperturbative analysis. *Nucl. Phys. B* **1996**, *466*, 189–258.
174. Kajantie, K.; Laine, M.; Rummukainen, K.; et al. Is there a hot electroweak phase transition at $m_H \gtrsim m_W$? *Phys. Rev. Lett.* **1996**, *77*, 2887–2890.

175. Laine, M.; Rummukainen, K. What's new with the electroweak phase transition? *Nucl. Phys. B Proc. Suppl.* **1999**, *73*, 180–185.
176. Ghiglieri, J.; Jackson, G.; Laine, M.; et al. Gravitational wave background from Standard Model physics: Complete leading order. *J. High Energy Phys.* **2020**, *2020*, 92.
177. McDonald, J. Electroweak baryogenesis and dark matter via a gauge singlet scalar. *Phys. Lett. B* **1994**, *323*, 339–346.
178. Espinosa, J.R.; Quiros, M. The Electroweak phase transition with a singlet. *Phys. Lett. B* **1993**, *305*, 98–105.
179. Espinosa, J.R.; Quiros, M. Novel Effects in Electroweak Breaking from a Hidden Sector. *Phys. Rev. D* **2007**, *76*, 076004.
180. Profumo, S.; Ramsey-Musolf, M.J.; Shaughnessy, G. Singlet Higgs phenomenology and the electroweak phase transition. *J. High Energy Phys.* **2007**, *2007*, 010.
181. Espinosa, J.R.; Konstandin, T.; Riva, F. Strong Electroweak Phase Transitions in the Standard Model with a Singlet. *Nucl. Phys.* **2012**, *B854*, 592–630.
182. Barger, V.; Chung, D.J.H.; Long, A.J.; et al. Strongly First Order Phase Transitions Near an Enhanced Discrete Symmetry Point. *Phys. Lett. B* **2012**, *710*, 1–7.
183. Cline, J.M.; Kainulainen, K. Electroweak baryogenesis and dark matter from a singlet Higgs. *J. Cosmol. Astropart. Phys.* **2013**, *2013*, 012.
184. Alanne, T.; Tuominen, K.; Vaskonen, V. Strong phase transition, dark matter and vacuum stability from simple hidden sectors. *Nucl. Phys. B* **2014**, *889*, 692–711.
185. Curtin, D.; Meade, P.; Yu, C.T. Testing Electroweak Baryogenesis with Future Colliders. *J. High Energy Phys.* **2014**, *11*, 127.
186. Vaskonen, V. Electroweak baryogenesis and gravitational waves from a real scalar singlet. *Phys. Rev. D* **2017**, *95*, 123515.
187. Kurup, G.; Perelstein, M. Dynamics of Electroweak Phase Transition In Singlet-Scalar Extension of the Standard Model. *Phys. Rev.* **2017**, *D96*, 015036.
188. Beniwal, A.; Lewicki, M.; Wells, J.D.; et al. Gravitational wave, collider and dark matter signals from a scalar singlet electroweak baryogenesis. *J. High Energy Phys.* **2017**, *08*, 108.
189. Niemi, L.; Schicho, P.; Tenkanen, T.V.I. Singlet-assisted electroweak phase transition at two loops. *Phys. Rev. D* **2021**, *103*, 115035. Erratum in *Phys. Rev. D* **2024**, *109*, 039902.
190. Lewicki, M.; Merchand, M.; Zych, M. Electroweak bubble wall expansion: gravitational waves and baryogenesis in Standard Model-like thermal plasma. *J. High Energy Phys.* **2022**, *2022*, 17.
191. Ellis, J.; Lewicki, M.; Merchand, M.; et al. The scalar singlet extension of the Standard Model: gravitational waves versus baryogenesis. *J. High Energy Phys.* **2023**, *2023*, 93.
192. Dev, P.S.B.; Ferrer, F.; Zhang, Y.; et al. Gravitational Waves from First-Order Phase Transition in a Simple Axion-Like Particle Model. *J. Cosmol. Astropart. Phys.* **2019**, *1911*, 006.
193. Craig, N.; Lou, H.K.; McCullough, M.; et al. The Higgs Portal Above Threshold. *J. High Energy Phys.* **2016**, *2016*, 127.
194. Morrissey, D.E.; Ramsey-Musolf, M.J. Electroweak baryogenesis. *New J. Phys.* **2012**, *14*, 125003.
195. Huang, F.P.; Qian, Z.; Zhang, M. Exploring dynamical CP violation induced baryogenesis by gravitational waves and colliders. *Phys. Rev.* **2018**, *D98*, 015014.
196. Azatov, A.; Barni, G.; Chakraborty, S.; et al. Ultra-relativistic bubbles from the simplest Higgs portal and their cosmological consequences. *J. High Energy Phys.* **2022**, *10*, 017.
197. Cline, J.M.; Friedlander, A.; He, D.M.; et al. Baryogenesis and gravity waves from a UV-completed electroweak phase transition. *Phys. Rev. D* **2021**, *103*, 123529.
198. Huet, P.; Nelson, A.E. CP violation and electroweak baryogenesis in extensions of the standard model. *Phys. Lett.* **1995**, *B355*, 229–235.
199. Cline, J.M.; Lemieux, P.A. Electroweak phase transition in two Higgs doublet models. *Phys. Rev.* **1997**, *D55*, 3873–3881.
200. Fromme, L.; Huber, S.J.; Seniuch, M. Baryogenesis in the two-Higgs doublet model. *J. High Energy Phys.* **2006**, *11*, 038.
201. Cline, J.M.; Kainulainen, K.; Trott, M. Electroweak Baryogenesis in Two Higgs Doublet Models and B meson anomalies. *J. High Energy Phys.* **2011**, *11*, 089.
202. Dorsch, G.C.; Huber, S.J.; No, J.M. A strong electroweak phase transition in the 2HDM after LHC8. *J. High Energy Phys.* **2013**, *10*, 029.
203. Dorsch, G.C.; Huber, S.J.; Mimasu, K.; et al. Echoes of the Electroweak Phase Transition: Discovering a second Higgs doublet through $A_0 \to ZH_0$. *Phys. Rev. Lett.* **2014**, *113*, 211802.
204. Kakizaki, M.; Kanemura, S.; Matsui, T. Gravitational waves as a probe of extended scalar sectors with the first order electroweak phase transition. *Phys. Rev.* **2015**, *D92*, 115007.
205. Dorsch, G.C.; Huber, S.J.; Konstandin, T.; et al. A Second Higgs Doublet in the Early Universe: Baryogenesis and Gravitational Waves. *J. Cosmol. Astropart. Phys.* **2017**, *1705*, 052.
206. Basler, P.; Krause, M.; Muhlleitner, M.; et al. Strong First Order Electroweak Phase Transition in the CP-Conserving 2HDM Revisited. *J. High Energy Phys.* **2017**, *2017*, 121.
207. Dorsch, G.C.; Huber, S.J.; Mimasu, K.; et al. The Higgs Vacuum Uplifted: Revisiting the Electroweak Phase Transition with a Second Higgs Doublet. *J. High Energy Phys.* **2017**, *12*, 086.

208. Basler, P.; Mühlleitner, M.; Wittbrodt, J. The CP-Violating 2HDM in Light of a Strong First Order Electroweak Phase Transition and Implications for Higgs Pair Production. *J. High Energy Phys.* **2018**, *2018*, 61.
209. Bernon, J.; Bian, L.; Jiang, Y. A new insight into the phase transition in the early Universe with two Higgs doublets. *J. High Energy Phys.* **2018**, *2018*, 151.
210. Huang, F.P.; Yu, J.H. Exploring inert dark matter blind spots with gravitational wave signatures. *Phys. Rev.* **2018**, *D98*, 095022.
211. Patel, H.H.; Ramsey-Musolf, M.J. Stepping Into Electroweak Symmetry Breaking: Phase Transitions and Higgs Phenomenology. *Phys. Rev.* **2013**, *D88*, 035013.
212. Chala, M.; Ramos, M.; Spannowsky, M. Gravitational wave and collider probes of a triplet Higgs sector with a low cutoff. *Eur. Phys. J.* **2019**, *C79*, 156.
213. Blinov, N.; Kozaczuk, J.; Morrissey, D.E.; et al. Electroweak Baryogenesis from Exotic Electroweak Symmetry Breaking. *Phys. Rev.* **2015**, *D92*, 035012.
214. Inoue, S.; Ovanesyan, G.; Ramsey-Musolf, M.J. Two-Step Electroweak Baryogenesis. *Phys. Rev.* **2016**, *D93*, 015013.
215. Blinov, N.; Kozaczuk, J.; Morrissey, D.E.; et al. Compressing the Inert Doublet Model. *Phys. Rev.* **2016**, *D93*, 035020.
216. Huber, S.J.; Konstandin, T.; Nardini, G.; et al. Detectable Gravitational Waves from Very Strong Phase Transitions in the General NMSSM. *J. Cosmol. Astropart. Phys.* **2016**, *1603*, 036.
217. Bian, L.; Guo, H.K.; Shu, J. Gravitational Waves, baryon asymmetry of the universe and electric dipole moment in the CP-violating NMSSM. *Chin. Phys.* **2018**, *C42*, 093106.
218. Demidov, S.V.; Gorbunov, D.S.; Kirpichnikov, D.V. Gravitational waves from phase transition in split NMSSM. *Phys. Lett.* **2018**, *B779*, 191–194.
219. Georgi, H.; Machacek, M. Doubly Charged Higgs Bosons. *Nucl. Phys.* **1985**, *B262*, 463–477.
220. Cort, L.; Garcia, M.; Quiros, M. Supersymmetric Custodial Triplets. *Phys. Rev.* **2013**, *D88*, 075010.
221. Garcia-Pepin, M.; Quiros, M. Strong electroweak phase transition from Supersymmetric Custodial Triplets. *J. High Energy Phys.* **2016**, *2016*, 177.
222. Zhang, X.M. Operators analysis for Higgs potential and cosmological bound on Higgs mass. *Phys. Rev.* **1993**, *D47*, 3065–3067.
223. Grojean, C.; Servant, G.; Wells, J.D. First-order electroweak phase transition in the standard model with a low cutoff. *Phys. Rev.* **2005**, *D71*, 036001.
224. Delaunay, C.; Grojean, C.; Wells, J.D. Dynamics of Non-renormalizable Electroweak Symmetry Breaking. *J. High Energy Phys.* **2008**, *2008*, 29.
225. Bodeker, D.; Fromme, L.; Huber, S.J.; et al. The Baryon asymmetry in the standard model with a low cut-off. *J. High Energy Phys.* **2005**, *2005*, 26.
226. Harman, C.P.D.; Huber, S.J. Does zero temperature decide on the nature of the electroweak phase transition? *J. High Energy Phys.* **2016**, *2016*, 5.
227. Damgaard, P.H.; Haarr, A.; O'Connell, D.; et al. Effective Field Theory and Electroweak Baryogenesis in the Singlet-Extended Standard Model. *J. High Energy Phys.* **2016**, *2016*, 107.
228. de Vries, J.; Postma, M.; van de Vis, J.; et al. Electroweak Baryogenesis and the Standard Model Effective Field Theory. *J. High Energy Phys.* **2018**, *2018*, 89.
229. Chala, M.; Krause, C.; Nardini, G. Signals of the electroweak phase transition at colliders and gravitational wave observatories. *J. High Energy Phys.* **2018**, *2018*, 62.
230. Huber, S.J.; Konstandin, T. Production of gravitational waves in the nMSSM. *J. Cosmol. Astropart. Phys.* **2008**, *2008*, 17.
231. Huang, F.P.; Wan, Y.; Wang, D.G.; et al. Hearing the echoes of electroweak baryogenesis with gravitational wave detectors. *Phys. Rev.* **2016**, *D94*, 041702.
232. Iso, S.; Okada, N.; Orikasa, Y. Classically conformal B^- L extended Standard Model. *Phys. Lett. B* **2009**, *676*, 81–87.
233. Iso, S.; Okada, N.; Orikasa, Y. The minimal B-L model naturally realized at TeV scale. *Phys. Rev. D* **2009**, *80*, 115007.
234. Escudero, M.; Witte, S.J.; Rius, N. The dispirited case of gauged $\mathrm{U}(1)_{B-L}$ dark matter. *J. High Energy Phys.* **2018**, *2018*, 190.
235. Dasgupta, A.; Dev, P.S.B.; Ghoshal, A.; et al. Gravitational wave pathway to testable leptogenesis. *Phys. Rev. D* **2022**, *106*, 075027.
236. Jinno, R.; Takimoto, M. Probing a classically conformal B-L model with gravitational waves. *Phys. Rev. D* **2017**, *95*, 015020.
237. Marzo, C.; Marzola, L.; Vaskonen, V. Phase transition and vacuum stability in the classically conformal B–L model. *Eur. Phys. J. C* **2019**, *79*, 601.
238. Sagunski, L.; Schicho, P.; Schmitt, D. Supercool exit: Gravitational waves from QCD-triggered conformal symmetry breaking. *Phys. Rev. D* **2023**, *107*, 123512.
239. Creminelli, P.; Nicolis, A.; Rattazzi, R. Holography and the electroweak phase transition. *J. High Energy Phys.* **2002**, *2002*, 51.
240. Randall, L.; Servant, G. Gravitational waves from warped spacetime. *J. High Energy Phys.* **2007**, *2007*, 54.
241. Nardini, G.; Quiros, M.; Wulzer, A. A Confining Strong First-Order Electroweak Phase Transition. *J. High Energy Phys.* **2007**, *2007*, 077.

242. Hassanain, B.; March-Russell, J.; Schvellinger, M. Warped Deformed Throats have Faster (Electroweak) Phase Transitions. *J. High Energy Phys.* **2007**, *10*, 089.
243. Konstandin, T.; Nardini, G.; Quiros, M. Gravitational Backreaction Effects on the Holographic Phase Transition. *Phys. Rev. D* **2010**, *82*, 083513.
244. Konstandin, T.; Servant, G. Cosmological Consequences of Nearly Conformal Dynamics at the TeV scale. *J. Cosmol. Astropart. Phys.* **2011**, *12*, 009.
245. Bunk, D.; Hubisz, J.; Jain, B. A Perturbative RS I Cosmological Phase Transition. *Eur. Phys. J. C* **2018**, *78*, 78.
246. Dillon, B.M.; El-Menoufi, B.K.; Huber, S.J.; et al. Rapid holographic phase transition with brane-localized curvature. *Phys. Rev. D* **2018**, *98*, 086005.
247. von Harling, B.; Servant, G. QCD-induced Electroweak Phase Transition. *J. High Energy Phys.* **2018**, *2018*, 159.
248. Megías, E.; Nardini, G.; Quirós, M. Cosmological Phase Transitions in Warped Space: Gravitational Waves and Collider Signatures. *J. High Energy Phys.* **2018**, *2018*, 95.
249. Fujikura, K.; Nakai, Y.; Yamada, M. A more attractive scheme for radion stabilization and supercooled phase transition **2020**, *2020*, 111.
250. Panico, G.; Wulzer, A. *The Composite Nambu-Goldstone Higgs*; Springer: Cham, Switzerland, 2016; Volume 913.
251. Grojean, C.; Matsedonskyi, O.; Panico, G. Light top partners and precision physics. *J. High Energy Phys.* **2013**, *2013*, 160.
252. Csáki, C.; Geller, M.; Telem, O. Tree-level Quartic for a Holographic Composite Higgs. *J. High Energy Phys.* **2018**, *2018*, 134.
253. Grinstein, B.; Trott, M. Electroweak Baryogenesis with a Pseudo-Goldstone Higgs. *Phys. Rev. D* **2008**, *78*, 075022.
254. Schwaller, P. Gravitational Waves from a Dark Phase Transition. *Phys. Rev. Lett.* **2015**, *115*, 181101.
255. Jaeckel, J.; Khoze, V.V.; Spannowsky, M. Hearing the signal of dark sectors with gravitational wave detectors. *arXiv* **2016**, arXiv:1602.03901.
256. Chala, M.; Nardini, G.; Sobolev, I. Unified explanation for dark matter and electroweak baryogenesis with direct detection and gravitational wave signatures. *arXiv* **2016**, arXiv:1605.08663.
257. Addazi, A. Limiting First Order Phase Transitions in Dark Gauge Sectors from Gravitational Waves experiments. *Mod. Phys. Lett. A* **2017**, *32*, 1750049.
258. Baldes, I. Gravitational waves from the asymmetric-dark-matter generating phase transition. *J. Cosmol. Astropart. Phys.* **2017**, *2017*, 028.
259. Addazi, A.; Marciano, A. Gravitational waves from dark first order phase transitions and dark photons. *Chin. Phys. C* **2018**, *42*, 023107.
260. Tsumura, K.; Yamada, M.; Yamaguchi, Y. Gravitational wave from dark sector with dark pion. *J. Cosmol. Astropart. Phys.* **2017**, *2017*, 044.
261. Aoki, M.; Goto, H.; Kubo, J. Gravitational Waves from Hidden QCD Phase Transition. *Phys. Rev. D* **2017**, *96*, 075045.
262. Croon, D.; White, G. Exotic Gravitational Wave Signatures from Simultaneous Phase Transitions. *J. High Energy Phys.* **2018**, *2018*, 210.
263. Croon, D.; Sanz, V.; White, G. Model Discrimination in Gravitational Wave spectra from Dark Phase Transitions. *J. High Energy Phys.* **2018**, *2018*, 203.
264. Baldes, I.; Garcia-Cely, C. Strong gravitational radiation from a simple dark matter model. *J. High Energy Phys.* **2019**, *2019*, 190.
265. Madge, E.; Schwaller, P. Leptophilic dark matter from gauged lepton number: Phenomenology and gravitational wave signatures. *J. High Energy Phys.* **2019**, *2019*, 48.
266. Breitbach, M.; Kopp, J.; Madge, E.; et al. Dark, Cold, and Noisy: Constraining Secluded Hidden Sectors with Gravitational Waves. *J. Cosmol. Astropart. Phys.* **2019**, *2019*, 007.
267. Fairbairn, M.; Hardy, E.; Wickens, A. Hearing without seeing: gravitational waves from hot and cold hidden sectors. *J. High Energy Phys.* **2019**, *2019*, 44.
268. Baker, M.J.; Kopp, J. Dark Matter Decay between Phase Transitions at the Weak Scale. *Phys. Rev. Lett.* **2017**, *119*, 061801.
269. Baker, M.J.; Breitbach, M.; Kopp, J.; et al. Dynamic Freeze-In: Impact of Thermal Masses and Cosmological Phase Transitions on Dark Matter Production. *J. High Energy Phys.* **2017**, *119*, 061801.
270. Greljo, A.; Opferkuch, T.; Stefanek, B.A. Gravitational Imprints of Flavor Hierarchies *Phys. Rev. Lett.* **2019**, *124*, 171802.
271. Delle Rose, L.; Panico, G.; Redi, M.; et al. Gravitational Waves from Supercool Axions. *J. High Energy Phys.* **2020**, *2020*, 25.
272. Baratella, P.; Pomarol, A.; Rompineve, F. The Supercooled Universe. *J. High Energy Phys.* **2019**, *2019*, 100.
273. Ferreira, R.Z.; Notari, A.; Pujolas, O.; et al. Gravitational waves from domain walls in Pulsar Timing Array datasets. *J. Cosmol. Astropart. Phys.* **2023**, *2023*, 001.
274. Holdom, B.; Peskin, M.E. Raising the Axion Mass. *Nucl. Phys. B* **1982**, *208*, 397–412.
275. Treiman, S.B.; Wilczek, F. Axion Emission in Decay of Excited Nuclear States. *Phys. Lett. B* **1978**, *74*, 381–383.
276. Dimopoulos, S. A Solution of the Strong CP Problem in Models With Scalars. *Phys. Lett. B* **1979**, *84*, 435–439.
277. Tye, S.H.H. A Superstrong Force With a Heavy Axion. *Phys. Rev. Lett.* **1981**, *47*, 1035.

278. Holdom, B. Strong QCD at High-energies and a Heavy Axion. *Phys. Lett. B* **1985**, *154*, 316.
279. Flynn, J.M.; Randall, L. A Computation of the Small Instanton Contribution to the Axion Potential. *Nucl. Phys. B* **1987**, *293*, 731–739.
280. Choi, K.; Do Kim, H. Small instanton contribution to the axion potential in supersymmetric models. *Phys. Rev. D* **1999**, *59*, 072001.
281. Agrawal, P.; Howe, K. Factoring the Strong CP Problem. *arXiv* **2017**, arXiv:1710.04213.
282. Kitano, R.; Yin, W. Strong CP problem and axion dark matter with small instantons. *J. High Energy Phys.* **2021**, *2021*, 78.
283. Rubakov, V.A. Grand unification and heavy axion. *J. Exp. Theor. Phys. Lett.* **1997**, *65*, 621–624.
284. Gherghetta, T.; Nagata, N.; Shifman, M. A Visible QCD Axion from an Enlarged Color Group. *Phys. Rev. D* **2016**, *93*, 115010.
285. Gherghetta, T.; Nguyen, M.D. A Composite Higgs with a Heavy Composite Axion. *J. High Energy Phys.* **2020**, *2020*, 94.
286. Berezhiani, Z.; Gianfagna, L.; Giannotti, M. Strong CP problem and mirror world: The Weinberg-Wilczek axion revisited. *Phys. Lett. B* **2001**, *500*, 286–296.
287. Dimopoulos, S.; Hook, A.; Huang, J.; et al. A collider observable QCD axion. *J. High Energy Phys.* **2016**, *2016*, 52.
288. Hook, A.; Kumar, S.; Liu, Z.; et al. High Quality QCD Axion and the LHC. *Phys. Rev. Lett.* **2020**, *124*, 221801.
289. Sikivie, P. Axions, Domain Walls and the Early Universe. *Phys. Rev. Lett.* **1982**, *48*, 1156–1159.
290. Schwarz, D.J.; Stuke, M. Lepton asymmetry and the cosmic QCD transition. *arXiv* **2009**, arXiv:0906.3434
291. Wygas, M.M.; Oldengott, I.M.; Bödeker, D.; et al. Cosmic QCD Epoch at Nonvanishing Lepton Asymmetry. *Phys. Rev. Lett.* **2018**, *121*, 201302.
292. Middeldorf-Wygas, M.M.; Oldengott, I.M.; Bödeker, D.; et al. Cosmic QCD transition for large lepton flavor asymmetries. *Phys. Rev. D* **2022**, *105*, 123533.
293. Chatterjee, A.; Frasca, M.; Ghoshal, A.; et al. Finite temperature QCD crossover at non-zero chemical potential: A Dyson–Schwinger approach. *Nucl. Phys. B* **2025**, *1017*, 116972.
294. Ekstedt, A.; Schicho, P.; Tenkanen, T.V.I. DRalgo: A package for effective field theory approach for thermal phase transitions. *Comput. Phys. Commun.* **2023**, *288*, 108725.
295. Ekstedt, A.; Schicho, P.; Tenkanen, T.V.I. Cosmological phase transitions at three loops: the final verdict on perturbation theory **2024**. *Phys. Rev. D* **2024**, *110*, 096006.
296. Kainulainen, K.; Keus, V.; Niemi, L.; et al. On the validity of perturbative studies of the electroweak phase transition in the Two Higgs Doublet model. *J. High Energy Phys.* **2019**, *2019*, 75.
297. Gould, O.; Kozaczuk, J.; Niemi, L.; et al. Nonperturbative analysis of the gravitational waves from a first-order electroweak phase transition. *Phys. Rev. D* **2019**, *100*, 115024.
298. Niemi, L.; Patel, H.H.; Ramsey-Musolf, M.J.; et al. Electroweak phase transition in the real triplet extension of the SM: Dimensional reduction. *Phys. Rev. D* **2019**, *100*, 035002.
299. Croon, D.; Gould, O.; Schicho, P.; et al. Theoretical uncertainties for cosmological first-order phase transitions. *J. High Energy Phys.* **2021**, *2021*, 55.
300. Kierkla, M.; Swiezewska, B.; Tenkanen, T.V.I.; et al. Gravitational waves from supercooled phase transitions: dimensional transmutation meets dimensional reduction. *J. High Energy Phys.* **2024**, *2024*, 234.
301. Schicho, P.M.; Tenkanen, T.V.I.; Österman, J. Robust approach to thermal resummation: Standard Model meets a singlet. *J. High Energy Phys.* **2021**, *2021*, 130.
302. Gould, O.; Tenkanen, T.V.I. Perturbative effective field theory expansions for cosmological phase transitions. *J. High Energy Phys.* **2024**, *2024*, 48.
303. Lewicki, M.; Merchand, M.; Sagunski, L.; et al. Impact of theoretical uncertainties on model parameter reconstruction from GW signals sourced by cosmological phase transitions *Phys. Rev. D* **2024**, *110*, 023538.
304. Banerjee, U.; Chakraborty, S.; Prakash, S.; et al. The feasibility of ultra-relativistic bubbles in SMEFT **2024**. *Phys. Rev. D* **2024**, *110*, 055002.
305. Coleman, S.R. The Fate of the False Vacuum. 1. Semiclassical Theory. *Phys. Rev. D* **1977**, *15*, 2929–2936.
306. Callan, C.G.; Coleman, S.R. The Fate of the False Vacuum. 2. First Quantum Corrections. *Phys. Rev. D* **1977**, *16*, 1762–1768.
307. Linde, A.D. Fate of the False Vacuum at Finite Temperature: Theory and Applications. *Phys. Lett. B* **1981**, *100*, 37–40.
308. Linde, A.D. Decay of the False Vacuum at Finite Temperature. *Nucl. Phys. B* **1983**, *216*, 421–445.
309. Turner, M.S.; Weinberg, E.J.; Widrow, L.M. Bubble nucleation in first order inflation and other cosmological phase transitions. *Phys. Rev. D* **1992**, *46*, 2384–2403.
310. Megevand, A.; Ramirez, S. Bubble nucleation and growth in very strong cosmological phase transitions. *Nucl. Phys. B* **2017**, *919*, 74–109,
311. Hindmarsh, M.B.; Lüben, M.; Lumma, J.; et al. Phase transitions in the early universe. *arXiv* **2021**, arXiv:2008.09136.
312. Ignatius, J.; Kajantie, K.; Kurki-Suonio, H.; et al. The growth of bubbles in cosmological phase transitions. *Phys. Rev. D* **1994**, *49*, 3854–3868,
313. Kurki-Suonio, H.; Laine, M. On bubble growth and droplet decay in cosmological phase transitions. *Phys. Rev. D* **1996**, *54*, 7163–7171.

314. Kurki-Suonio, H.; Laine, M. Supersonic deflagrations in cosmological phase transitions. *Phys. Rev. D* **1995**, *51*, 5431–5437.
315. Giese, F.; Konstandin, T.; van de Vis, J. Model-independent energy budget of cosmological first-order phase transitions—A sound argument to go beyond the bag model. *J. Cosmol. Astropart. Phys.* **2020**, *2020*, 057.
316. Available online: https://github.com/cosmoGW/cosmoGW (accessed on 10 November 2025).
317. Ekstedt, A.; Gould, O.; Hirvonen, J.; et al. How fast does the WallGo? A package for computing wall velocities in first-order phase transitions. *J. High Energy Phys.* **2025**, *2025*, 101.
318. Moore, G.D.; Prokopec, T. How fast can the wall move? A Study of the electroweak phase transition dynamics. *Phys. Rev. D* **1995**, *52*, 7182–7204.
319. Moore, G.D.; Prokopec, T. Bubble wall velocity in a first order electroweak phase transition. *Phys. Rev. Lett.* **1995**, *75*, 777–780.
320. Bodeker, D.; Moore, G.D. Can electroweak bubble walls run away? *arXiv* **2009**, arXiv:0903.4099.
321. Konstandin, T.; Nardini, G.; Rues, I. From Boltzmann equations to steady wall velocities. *arXiv* **2014**, arXiv:1407.3132.
322. Kozaczuk, J. Bubble Expansion and the Viability of Singlet-Driven Electroweak Baryogenesis. *J. High Energy Phys.* **2015**, *2015*, 135.
323. Höche, S.; Kozaczuk, J.; Long, A.J.; et al. Towards an all-orders calculation of the electroweak bubble wall velocity. *arXiv* **2021**, arXiv:2007.10343
324. Barroso Mancha, M.; Prokopec, T.; Swiezewska, B. Field-theoretic derivation of bubble-wall force. *arXiv* **2021**, arXiv:2005.10875.
325. Laurent, B.; Cline, J.M. First principles determination of bubble wall velocity. *Phys. Rev. D* **2022**, *106*, 023501.
326. Huber, S.J.; Sopena, M. An efficient approach to electroweak bubble velocities. *arXiv* **2013**, arXiv:1302.1044.
327. Friedlander, A.; Banta, I.; Cline, J.M.; et al. Wall speed and shape in singlet-assisted strong electroweak phase transitions. *Phys. Rev. D* **2021**, *103*, 055020.
328. Laurent, B.; Cline, J.M. Fluid equations for fast-moving electroweak bubble walls. *Phys. Rev. D* **2020**, *102*, 063516.
329. Dorsch, G.C.; Huber, S.J.; Konstandin, T. Bubble wall velocities in the Standard Model and beyond. *arXiv* **2018**, arXiv:1809.04907.
330. Jinno, R.; Takimoto, M. Gravitational waves from bubble dynamics: Beyond the Envelope. *arXiv* **2019**, arXiv:1707.03111.
331. Ellis, J.; Lewicki, M.; Vaskonen, V. Updated predictions for gravitational waves produced in a strongly supercooled phase transition. *arXiv* **2020**, arXiv:2007.15586.
332. Athron, P.; Balázs, C.; Morris, L. Supercool subtleties of cosmological phase transitions. *arXiv* **2023**, arXiv:2212.07559.
333. Ellis, J.; Lewicki, M.; No, J.M. On the Maximal Strength of a First-Order Electroweak Phase Transition and its Gravitational Wave Signal. *arXiv* **2019**, arXiv:1809.08242.
334. Child, H.L.; Giblin, J.T., Jr. Gravitational Radiation from First-Order Phase Transitions. *J. Cosmol. Astropart. Phys.* **2012**, *2012*, 001.
335. Jinno, R.; Konstandin, T.; Takimoto, M. Relativistic bubble collisions—A closer look. *J. Cosmol. Astropart. Phys.* **2019**, *2019*, 035.
336. Hindmarsh, M. Sound shell model for acoustic gravitational wave production at a first-order phase transition in the early Universe. *Phys. Rev. Lett.* **2018**, *120*, 071301.
337. Cai, R.G.; Wang, S.J.; Yuwen, Z.Y. Hydrodynamic sound shell model. *Phys. Rev. D* **2023**, *108*, L021502.
338. Roper Pol, A.; Procacci, S.; Caprini, C. Characterization of the gravitational wave spectrum from sound waves within the sound shell model. *Phys. Rev. D* **2024**, *109*, 063531.
339. Kosowsky, A.; Mack, A.; Kahniashvili, T. Gravitational radiation from cosmological turbulence. *Phys. Rev. D* **2002**, *66*, 024030.
340. Giombi, L.; Dahl, J.; Hindmarsh, M. Acoustic gravitational waves beyond leading order in bubble over Hubble radius. *arXiv* **2025**, arXiv:2504.08037.
341. Hindmarsh, M.; Huber, S.J.; Rummukainen, K.; et al. Gravitational waves from the sound of a first order phase transition. *Phys. Rev. Lett.* **2014**, *112*, 041301.
342. Jinno, R.; Konstandin, T.; Rubira, H. A hybrid simulation of gravitational wave production in first-order phase transitions. *J. Cosmol. Astropart. Phys.* **2021**, *2021*, 014.
343. Jinno, R.; Konstandin, T.; Rubira, H.; et al. Higgsless simulations of cosmological phase transitions and gravitational waves. *J. Cosmol. Astropart. Phys.* **2023**, *2023*, 011.
344. Caprini, C.; Jinno, R.; Konstandin, T.; et al. Gravitational waves from decaying sources in strong phase transitions. *arXiv* **2024**, arXiv:2409.03651.
345. Roper Pol, A.; Brandenburg, A.; Kahniashvili, T.; et al. The timestep constraint in solving the gravitational wave equations sourced by hydromagnetic turbulence. *Geophys. Astrophys. Fluid Dyn.* **2020**, *114*, 130–161.
346. Roper Pol, A.; Mandal, S.; Brandenburg, A.; et al. Polarization of gravitational waves from helical MHD turbulent sources. *J. Cosmol. Astropart. Phys.* **2022**, *2022*, 019.
347. Brandenburg, A.; Gogoberidze, G.; Kahniashvili, T.; et al. The scalar, vector, and tensor modes in gravitational wave turbulence simulations. *Class. Quantum Gravity* **2021**, *38*, 145002.

348. Correia, J.; Hindmarsh, M.; Rummukainen, K.; et al. Gravitational waves from strong first order phase transitions. *arXiv* **2025**, arXiv:2505.17824.
349. Sharma, R.; Dahl, J.; Brandenburg, A.; et al. Shallow relic gravitational wave spectrum with acoustic peak. *J. Cosmol. Astropart. Phys.* **2023**, *2023*, 042.
350. Dahl, J.; Hindmarsh, M.; Rummukainen, K.; et al. Decay of acoustic turbulence in two dimensions and implications for cosmological gravitational waves. *Phys. Rev. D* **2022**, *106*, 063511.
351. Brandenburg, A.; Johansen, A.; Bourdin, P.A.; et al. The Pencil Code, a modular MPI code for partial differential equations and particles: multipurpose and multiuser-maintained. *J. Open Source Softw.* **2021**, *6*, 2807.
352. Badger, C.; Fornal, B.; Martinovic, K.; et al. Probing early Universe supercooled phase transitions with gravitational wave data. *Phys. Rev. D* **2023**, *107*, 023511.
353. Caprini, C.; Figueroa, D.G.; Flauger, R.; et al. Reconstructing the spectral shape of a stochastic gravitational wave background with LISA *J. Cosmol. Astropart. Phys.* **2019**, *2019*, 017.
354. Flauger, R.; Karnesis, N.; Nardini, G.; et al. Improved reconstruction of a stochastic gravitational wave background with LISA. *J. Cosmol. Astropart. Phys.* **2021**, *01*, 059.
355. Torrado, J.; Lewis, A. Cobaya: Code for Bayesian Analysis of hierarchical physical models. *J. Cosmol. Astropart. Phys.* **2021**, *05*, 057.
356. Handley, W.J.; Hobson, M.P.; Lasenby, A.N. polychord: next-generation nested sampling. *Mon. Not. Roy. Astron. Soc.* **2015**, *453*, 4385–4399.
357. Handley, W.J.; Hobson, M.P.; Lasenby, A.N. PolyChord: nested sampling for cosmology. *Mon. Not. Roy. Astron. Soc.* **2015**, *450*, L61–L65.
358. Lewis, A. GetDist: a Python package for analysing Monte Carlo samples. *J. Cosmol. Astropart. Phys.* **2025**, *2025*, 025.
359. Gowling, C.; Hindmarsh, M. Observational prospects for phase transitions at LISA: Fisher matrix analysis. *J. Cosmol. Astropart. Phys.* **2021**, *2021*, 039.
360. Gowling, C.; Hindmarsh, M.; Hooper, D.C.; et al. Reconstructing physical parameters from template gravitational wave spectra at LISA: first order phase transitions. *J. Cosmol. Astropart. Phys.* **2023**, *2023*, 061.
361. Giese, F.; Konstandin, T.; van de Vis, J. Finding sound shells in LISA mock data using likelihood sampling. *J. Cosmol. Astropart. Phys.* **2021**, *2021*, 002.
362. Blasi, S.; Mariotti, A. Domain Walls Seeding the Electroweak Phase Transition. *Phys. Rev. Lett.* **2022**, *129*, 261303.